Effects of nonperturbatively improved dynamical fermions in QCD at fixed lattice spacing

C. R. Allton,[1] S. P. Booth,[2] K. C. Bowler,[3] J. Garden,[3] A. Hart,[3,4] D. Hepburn,[3] A. C. Irving,[5] B. Joó,[3] R. D. Kenway,[3] C. M. Maynard,[3] C. McNeile,[5] C. Michael,[5] S. M. Pickles,[3] J. C. Sexton,[6] K. J. Sharkey,[5] Z. Sroczynski,[3] M. Talevi,[3] M. Teper,[7] and H. Wittig[7,5]

(UKQCD Collaboration)

[1]*Department of Physics, University of Wales Swansea, Swansea SA2 8PP, Wales*
[2]*Edinburgh Parallel Computing Centre, University of Edinburgh, Edinburgh EH9 3JZ, Scotland*
[3]*Department of Physics & Astronomy, University of Edinburgh, Edinburgh EH9 3JZ, Scotland*
[4]*Department of Applied Mathematics and Theoretical Physics, University of Cambridge, Cambridge CB3 0WA, England*
[5]*Division of Theoretical Physics, Department of Mathematical Sciences, University of Liverpool, Liverpool L69 3BX, England*
[6]*School of Mathematics, Trinity College, Dublin 2, Ireland*
and Hitachi Dublin Laboratory, Dublin 2, Ireland
[7]*Theoretical Physics, University of Oxford, Oxford OX1 3NP, England*

(Received 30 July 2001; published 30 January 2002)

We present results for the static interquark potential, lightest glueballs, light hadron spectrum, and topological susceptibility using a nonperturbatively improved action on a $16^3\times 32$ lattice at a set of values of the bare gauge coupling and bare dynamical quark mass chosen to keep the lattice size fixed in physical units ($\sim$1.7 fm). By comparing these measurements with a matched quenched ensemble, we study the effects due to two degenerate flavors of dynamical quarks. With the greater control over residual lattice spacing effects which these methods afford, we find some evidence of charge screening and some minor effects on the light hadron spectrum over the range of quark masses studied ($M_{\rm PS}/M_V \geq 0.58$, where PS denotes pseudoscalar and V denotes vector). More substantial differences between quenched and unquenched simulations are observed in measurements of topological quantities.

DOI: 10.1103/PhysRevD.65.054502 PACS number(s): 11.15.Ha, 12.38.Gc

I. INTRODUCTION

Over recent years, considerable effort has gone into probing QCD beyond the quenched approximation. For recent reviews see [1–4], and for results using a different improvement scheme see [5]. Because of the impressive agreement of the quenched approximation (see, e.g., [6]) with experiment for the spectrum and other easily accessible quantities, the effects of dynamical quarks in these are expected to be quite small. It is difficult to isolate physical effects which are unambiguously due to their inclusion, in part because of the need for high statistics. On currently available machines this requires coarse lattices. The use of $O(a)$ nonperturbatively improved fermions has been suggested as a means of controlling and reducing discretization errors [7]. In an earlier paper [8], the first results of the UKQCD Collaboration using a preliminary value of the improvement coefficient $c_{\rm SW}$ were presented. It was found that the effective lattice spacing, as measured by Sommer's intermediate scale parameter r_0 [9], depended quite strongly on the bare quark mass at fixed gauge coupling. However, the effect of dynamical quarks on easily accessible physical observables was very weak and difficult to disentangle from those induced by other changes in the simulation parameters. Eventually, one might hope to perform detailed studies over the full space of parameters including bare gauge coupling, quark mass(es), and lattice volume. In the meantime, less ambitious studies may still serve as a guide to those regions of parameter space where physical effects may be found.

In this paper, we present the results of further simulations over a range of sea quark masses. For these simulations, we have used the final published values of the $O(a)$ improvement coefficient $c_{\rm SW}$ [7] and have attempted to reduce variations due to residual discretization errors and finite volume effects by working at fixed lattice spacing. In order to achieve the latter, we have used matching techniques described in an earlier work [10] to help obtain ensembles of configurations whose lattice spacings, as defined by the scale r_0, are as closely matched as practicable. We present results for the spectrum and potential on, or close to, a single fixed r_0 trajectory in the (β,κ) plane, which extends from quenched configurations ($\kappa=0$) to the lightest accessible sea quark mass. We choose r_0 to set the scale since it has no valence quark complications and is determined by intermediate scale properties of the static potential. These properties are expected to be less sensitive to charge screening (short-range) and string-breaking (long-range) effects arising from dynamical light quarks.

We interpret our results in the spirit of partial quenching. That is, we study chiral extrapolation in the valence quark masses of light hadron masses using both quenched and partially unquenched configurations. We find that, with the available statistics, the quality of these valence extrapolations is uniformly good. By studying the spectra so obtained, we search for evidence of the influence of light dynamical quarks. We also study the behavior of the topological susceptibility in the presence of dynamical quarks. Our data sample includes measurements made with equal valence and sea quark masses.

The plan of the rest of the paper is as follows. Section II contains brief details of the simulation methods and parameters. In Sec. III, we review the matching techniques used to set up simulations at similar lattice spacings. We present results in Sec. IV for the static potential in QCD and use it to define a lattice scale. In Sec. V, we present results for the light hadron spectrum including some measurements of the lightest glueball masses. Section VI contains results from topological charge and susceptibility measurements. Finally, our conclusions are summarized in Sec. VII.

Some preliminary results from these analyses have been presented elsewhere [11–16].

II. SIMULATIONS WITH IMPROVED WILSON FERMIONS

Details of our implementation of the hybrid Monte Carlo simulation algorithm [17] and its performance can be found in our earlier paper [8]. Here, we summarize for convenience some key features. For the lattice action we used a standard Wilson action for the gauge fields together with the Sheikholeslami-Wohlert (SW) $O(a)$-improved Wilson gauge-fermion action [18]:

$$S[U,\overline{\psi},\psi]=S_G[U]+S_F[U,\overline{\psi},\psi], \tag{1}$$

where

$$S_G[U]=\beta W_{\Box}=\beta\sum_P\ (1-\tfrac{1}{3}\mathrm{Re\,Tr}\,U_P) \tag{2}$$

and

$$S_F[U,\overline{\psi},\psi]=S_F^W[U,\overline{\psi},\psi] + c_{\mathrm{SW}}\frac{i\kappa}{2}\sum_{x,\mu,\nu}\ \overline{\psi}(x)\sigma_{\mu\nu}F_{\mu\nu}(x)\psi(x). \tag{3}$$

Here, U_P is the usual directed product of gauge link variables and S_F^W is the standard Wilson fermion action,

$$S_F^W=\sum_x\ \overline{\psi}(x)\psi(x)-\kappa\sum_{x,\mu}\ [\overline{\psi}(x)(r-\gamma_\mu)U_\mu(x)\psi(x+\hat{\mu}) + \overline{\psi}(x+\hat{\mu})(r+\gamma_\mu)U_\mu^\dagger(x)\psi(x)] \tag{4}$$

with the Wilson parameter chosen as $r=1$. The spin matrix is $\sigma_{\mu\nu}=(i/2)[\gamma_\mu,\gamma_\nu]$, and $F_{\mu\nu}(x)$ is the field strength tensor

$$F_{\mu\nu}(x)=\tfrac{1}{8}[f_{\mu\nu}(x)-f_{\mu\nu}^\dagger(x)], \tag{5}$$

where $f_{\mu\nu}(x)=U_{\mu\nu}(x)+U_{\nu,-\mu}(x)+U_{-\nu,-\mu}(x)+U_{-\nu,\mu}(x)$ is the sum of four similarly oriented (open) plaquettes around a site, x.

Beyond tree level, the improvement coefficient c_{SW} is a function of the gauge coupling β ($\equiv 6/g^2$). In the studies reported here, we have used those values determined nonperturbatively by the Alpha Collaboration and summarized by an interpolation formula [7]. For example, at $\beta=5.20$ we have used[1] $c_{\mathrm{SW}}=2.0171$.

We have used two degenerate flavors of dynamical quarks in these simulations. The bare quark mass is controlled by the hopping parameter κ. Restoration of (spontaneously broken) chiral symmetry requires extrapolation in κ to the critical value κ_{crit} at which the pion is effectively massless. As discussed above, we will often discuss the situation encountered in the quenched approximation, where the dynamical (sea) quark mass parameter (κ^{sea}) is fixed (at 0 in the quenched case) while the chiral extrapolation is performed in the valence mass parameter (κ^{val}) only. This is often referred to as a partially quenched approximation. It is particularly relevant where the dynamical quark mass is still quite heavy and where there is no realistic prospect of approaching the (degenerate) light quark chiral limit in both parameters.

A. Simulation parameters

Since these simulations were the first to be done on a reasonably large lattice ($16^3\times 32$) using the fully improved value of c_{SW}, there was little guidance available on the choice of simulation parameters. We chose $\beta=5.20$ as the lowest value at which a reliable value of c_{SW} was available [7]. The aim was to obtain as large a physical volume as practicable with the available computing resource. The use of an improved action was expected to offset (at least partially) the relatively coarse lattice spacing which this implied. Equilibration was carried out through a sequence of dynamical quark masses: $\kappa^{\mathrm{sea}}=0.130\,00$, $0.133\,50$, $0.134\,00$, $0.134\,50$, to $0.135\,00$. The first production run was then carried out at $\kappa^{\mathrm{sea}}=0.135\,00$ starting at trajectory number 10010, where trajectories were of unit length. Configurations were stored after every 10 trajectories, although a larger separation was used for most operator measurements (see below).

Further simulations at higher quark masses ($\kappa^{\mathrm{sea}}=0.134\,50$ and $0.134\,00$) and slightly shifted β were then performed. The shifts in β were estimated using the methods described in Sec. III and were designed to maintain a constant lattice spacing as defined by r_0.

To complete the comparison of unquenching effects, we performed pure gauge simulations using a standard update algorithm, heat bath with overrelaxation. Again, the β value was chosen to keep r_0 at the value measured on the ensemble obtained at $(\beta,\kappa^{\mathrm{sea}})=(5.20,0.135\,00)$. The only exceptional configuration found was within the quenched configurations, and this was only apparent for one of the κ^{val} studied. This configuration was excluded from further analyses.

An additional substantial, but unmatched, simulation was then performed at $(\beta,\kappa^{\mathrm{sea}})=(5.20,0.135\,50)$. This ensemble

[1]Although the effect of $O(a)$ improvement is not expected to be as sensitive as the quoted number of significant figures suggests, the action and lattice observables do depend quite strongly on this parameter. For reasons of reproducibility we have therefore used a four-decimal place representation of the c_{SW} formula in generating configurations.

TABLE I. Summary of simulation parameters and statistics used in the computation of the static potential and light hadron spectrum.

β	c_{SW}	No. of Conf.	κ^{sea}	κ^{val}				
5.20	2.0171	244	0.13565	0.13565				
5.20	2.0171	832	0.1355	0.1355	0.1350	0.1345	0.1340	
5.20	2.0171	600	0.1350	0.1350	0.1345	0.1340	0.1335	
5.26	1.9497	404	0.1345	0.1350	0.1345	0.1340	0.1335	
5.29	1.9192	404	0.1340	0.1350	0.1345	0.1340	0.1335	
5.93	1.82	623	0	0.1339	0.1337	0.1334	0.1332	0.1327

of configurations was analyzed along with the matched ensembles providing further information on behavior at light quark mass. A simulation at even lighter quark mass ($\kappa^{sea}=0.135\,65$) was begun. Where relevant, some preliminary results are presented here. Table I contains a summary of the run parameters for each ensemble.

The bulk of the simulations were carried out in double precision. This followed initial concerns over the effect of rounding errors on reversibility. Detailed analyses of these and related effects have been carried out and have been reported elsewhere [19]. This work shows that, at least for the present volumes and step lengths, the algorithm is reversible and stable for all practical purposes, even when implemented in single precision.

B. Autocorrelations

We made autocorrelation measurements from the average plaquette value measurements on every trajectory. The methods used were those described in detail in our earlier paper [8]. As shown in Table II, the observable autocorrelation (from the plaquette) is of order 20 and so we have adopted a separation of 40 trajectories as standard in the analysis which follows. Nevertheless, we keep in mind that subtle longer-term autocorrelations, not directly measurable, may still be present and so we have done additional checks on our statistical error estimates by rebinning the measurements. In the present data sample, we have not found any evidence of such correlations.

Further measurements of the integrated autocorrelation time have been attempted for the potential (Sec. IV) and the scalar glueball (Sec. V G). At the lightest quark mass ($\kappa^{sea}=0.135\,65$), autocorrelations were estimated from effective-mass (potential-energy) measurements made every 20 trajectories at various lattice distances ($r/a=1-5$) and Euclidean times ($t/a=3-5$). The measured integrated autocorrelation times varied from 10 to 20 trajectories with large errors (typically ± 8). For the scalar glueball, the integrated autocorrelation time for effective masses was in the range 25–30 at $\kappa^{sea}=0.135\,00$ and $0.135\,50$.

TABLE II. Comparison of integrated autocorrelation times τ^{int} for the average plaquette measured in the present simulations with those in previous simulations at $\beta=5.20$, $c_{SW}=1.76$.

$L^3\cdot T$	β	c_{SW}	κ^{sea}	Traj. no.	τ^{int}
$16^3\cdot 32$	5.20	2.0171	0.13565	2400	13(5)
	5.20	2.0171	0.13550	8000	14(1)
	5.20	2.0171	0.13500	6000	16(3)
	5.26	1.9497	0.13450	6000	18(3)
	5.29	1.9192	0.13400	5000	25(7)
$16^3\cdot 24$	5.20	1.76	0.1390	3800	37(3)
	5.20	1.76	0.1395	3200	27(18)
	5.20	1.76	0.1398	3000	32(8)

It is noteworthy that the autocorrelation is significantly *less* in the current simulations than in our previous runs [8] at comparable quark masses but different c_{SW}. The current simulations use the fully nonperturbatively improved value of c_{SW}. It is further noted that τ^{int} appears to *decrease*, if anything, with decreasing quark mass. This is contrary to the simple expectation that, as the lattice correlation length (typically given by the inverse pion mass) increases, then so should the correlation in computer time. A similar effect is evident in the decorrelation properties of the topological charge (see Sec. VI). It is possible to reproduce such behavior in simple models. The integrated autocorrelation time, which determines the size of the errors, can decrease even in the presence of increasingly long correlation modes simply due to increased noise induced by dominant short correlation modes.

To illustrate this point, consider first the following simple model consisting of a single Markov chain $x(t)$, $t=0,1,2,\ldots$:

$$x(t)=ax(t-1)+z(t), \quad x(0)=0, \tag{6}$$

where the $z(t)$ are uncorrelated Gaussian noise of unit variance and $0<a<1$. It is simple to show that, for sufficiently long chains,

$$\rho_x(t)=a^t\equiv e^{-t/\tau^{exp}(x)} \tag{7}$$

and so

$$\tau^{exp}(x)=-\ln a, \quad \tau^{int}(x)=\frac{1}{2}\,\frac{1+a}{1-a}. \tag{8}$$

Here $\rho_x(t)$ is the normalized autocorrelation function for the observable x. The corresponding results for finite length chains are also calculable, so one can study the effects of

using limited statistics to estimate autocorrelation times. Here we stick to the infinite chain approximation. For $a \lesssim 1$ [i.e., for large $\tau^{\rm exp}(x)$],

$$\tau^{\rm int}(x) = \tau^{\rm exp}(x) + 1/[12\tau^{\rm exp}(x)] + O[(\tau^{\rm exp})^{-3}]. \quad (9)$$

Real hybrid Monte Carlo (HMC) data for $\rho(t)$ do not, of course, show a simple exponential behavior and so it is useful to consider the next simplest model, which contains two independent correlation modes with relative coupling strength r:

$$X(t) = x_1(t) + r x_2(t),$$
$$x_1(t) = a_i x_i(t-1) + z_i(t) \quad (i=1,2). \quad (10)$$

The integrated autocorrelation time for $X(t)$ is given by

$$\tau^{\rm int}(X) = \eta_1 \tau^{\rm int}(x_1) + \eta_2 \tau^{\rm int}(x_2), \quad (11)$$

where

$$\eta_1 + \eta_2 = 1, \quad \eta_2 = \frac{r^2(1-a_1^2)}{1-a_2^2+r^2(1-a_1^2)}. \quad (12)$$

Thus the relation between the integrated autocorrelation time and the actual correlations present in X_t is no longer straightforward. There may be quite long correlations present $[\tau^{\rm exp}(x_2) \gg \tau^{\rm exp}(x_1)]$ but, depending on the relative strength of the modes (given by r), the ''weighted average'' represented by the above formula can give a result bearing no relation to either $\tau^{\rm exp}(x_1)$ or $\tau^{\rm exp}(x_2)$.

The possibility of such behavior makes it essential to check decorrelation for individual observables explicitly using binning techniques.

C. Finite-size effects

In retrospect, the value of $\kappa^{\rm sea} = 0.135\,00$ turned out to be somewhat conservative, in that the corresponding ratio of $M_{\rm PS}/M_V$ (where PS denotes pseudoscalar and V denotes vector) is quite large (0.70, see Sec. V). The choice was based on preliminary estimates of the limiting algorithm performance and on measurements of the effective lattice spacing as described in Sec. IV. It was felt that decreasing the quark mass further would decrease the effective lattice size to a point where finite-size effects would become a problem. In our earlier analysis of finite-size effects (at least as far as they affect the potential and light hadron spectrum for $M_{\rm PS}/M_V \gtrsim 0.7$), we found that such effects were negligible provided

$$L/r_0 \gtrsim 3.2. \quad (13)$$

This corresponds to a spatial extent of around 1.6 fm and is satisfied by all but our lightest quark mass dataset, as shown in Table III. Further investigations may be called for, given the concerns over the baryon mass spectrum noted in [5] (see Sec. V C).

TABLE III. Measures of finite volume effects in simulations.

(β,κ)	L/r_0	LM_π
(5.20,0.13565)	3.07 (3)	4.18 (5)
(5.20,0.13550)	3.17 (3)	4.70 (6)
(5.20,0.13500)	3.37 (3)	6.48 (8)
(5.26,0.13450)	3.40 (4)	8.14 (3)
(5.29,0.13400)	3.32 (3)	9.23 (4)

III. MATCHING SIMULATION PARAMETERS

In a previous paper [10], we have described techniques which allow one to use unbiased stochastic estimates of the logarithm of the fermion determinant to determine, approximately, curves of constant observable in the space of simulation parameters.

A. Determination of fixed observable curves

The approximate character of the formalism arises from two sources. First, the log of the fermion determinant is only determined stochastically on each configuration and the corresponding fluctuations are proportional to the lattice volume. Second, a linear approximation is used when dealing with small changes so that these curves may only be determined locally. In the present application, the parameter space of interest is the (β,κ) plane and the observable of interest is the QCD static potential scale parameter r_0 (see Sec. IV).

To first order in small parameter changes $(\delta\beta,\delta\kappa)$, the shift in the lattice operator F is given by [10]

$$\langle \delta F \rangle = \left(\langle \tilde{F} \tilde{W}_\Box \rangle + \left\langle \tilde{F} \frac{\partial \tilde{T}}{\partial c_{\rm SW}} \right\rangle \dot{c}_{\rm SW} \right) \delta\beta + \left\langle \tilde{F} \frac{\partial \tilde{T}}{\partial \kappa} \right\rangle \delta\kappa. \quad (14)$$

The quantity

$$\dot{c}_{\rm SW} = \frac{dc_{\rm SW}}{d\beta}$$

is well determined [7] and so the identification of constant F curves

$$\langle \delta \tilde{F} \rangle = 0 \quad (15)$$

reduces to measuring correlations of the form

$$\langle \tilde{F} \tilde{W}_\Box \rangle \quad \text{and} \quad \langle \tilde{F}\, \delta\tilde{T} \rangle. \quad (16)$$

Here, $\langle \tilde{A} \rangle$ denotes the connected part $\langle A - \langle A \rangle \rangle$ of the operator A. We refer readers to [10] for a detailed discussion of the stochastic evaluation of $T \equiv \mathrm{Tr\,Ln}\, M^\dagger M$. Here, M is the fermion matrix including the $O(a)$ improvement term. The methods are based on a Lánczos implementation of Gaussian quadrature [20]. Recent progress in understanding the nature of roundoff errors in the finite arithmetic Lánczos process assures us that this application of the Lánczos process, unlike the basic algorithm itself, is highly stable with respect to roundoff [21].

B. Matching r_0

Detailed tests of the matching procedures have been carried out using the average plaquette, which is very accurately measured, and a variety of Wilson loops [10]. Some tests using r_0 were also carried out successfully on modest-sized lattices. The present work represents the first application, in earnest, to production-size lattices. Since the fluctuations in T are extensive quantities, we expect there will be a limit on the size of lattices where usefully accurate matching estimates may be made with a given amount of work. The work required has been analyzed in some detail in [10].

The correlations (16) require measurements of F on each configuration. These are available for operators such as Wilson loops but not for physical quantities such as hadron masses and r_0. Rather than determine the fixed r_0 curve directly using Eq. (15), we use Eq. (14) to estimate the required gauge correlators at nearby points in parameter space. We then extract the potential, and hence r_0/a, at the nearby parameter values from these ''shifted correlators.'' This allows estimates of the partial derivatives with respect to β and κ and hence the shift $\delta\beta_\kappa$ required to compensate for a particular change in $\kappa^{\rm sea}$,

$$\delta\beta_\kappa = \frac{\partial F}{\partial \kappa^{\rm sea}} \Big/ \frac{\partial F}{\partial \beta}\, \delta\kappa^{\rm sea}, \tag{17}$$

where, in the present application,[2] $F=\hat{r}_0 \equiv r_0/a$.

Using an ensemble of 100 configurations at $(\beta,\kappa)=(5.2,0.1350)$ for all correlator measurements, we estimated that a shift of

$$\delta\beta = 0.057 \pm 0.033$$

would be required so as to match the value of $\hat{r}_0$ at $(5.2+\delta\beta,0.1345)$ with that at $(\beta,\kappa)=(5.2,0.1350)$. A simulation run at $(\beta,\kappa)=(5.26,0.1345)$ confirms that r_0, and hence the effective lattice spacing, is indeed well matched (see Table V).

However, it is clear from the size of the statistical errors that estimates of $\delta\beta$ obtained on these configurations cannot be relied upon, in general, to predict matched parameters with great accuracy without further checks. The level of success in achieving $\hat{r}_0$ matching can be gauged from Table V.

The above methods for matching parameters are only applicable for small shifts. To obtain the shift for matching quenched simulations ($\delta\kappa=-\kappa$), we have used tabulated values [22] of $\hat{r}_0$ (lattice spacing a) to provide an initial estimate. Since there are systematic differences arising from slightly differing methods for extracting the potentials and $\hat{r}_0$ (see Sec. IV), we used this only as an initial guide. Following direct measurement of $\hat{r}_0$ with our own techniques, we then made a further small shift in β. The results are shown in the next section.

[2]Here, and in what follows, we use the notation $\hat{A}$ to denote a physical quantity A expressed in lattice units.

IV. THE QCD STATIC POTENTIAL

We have determined the static interquark potential $V(\mathbf{r})$ using standard methods and used it to search for signs of charge screening and string breaking, as well as to determine the physical scale.

A. Extraction of the potential

The methods follow those originally proposed by Michael and collaborators [23,24]. A variational basis of generalized Wilson loops is constructed from gauge links which are ''fuzzed'' in the spatial directions [25]. The spatial paths between the static sources include a limited number of off-axis directions as well as those along the lattice axes (see the lower half of Table IV). A transfer-matrix formalism is then used to extract the Euclidean time energy eigenstates which are related to solutions of the generalized eigenvalue equation

$$W_{ij}(\boldsymbol{r},t)\,\phi(\boldsymbol{r})^{(k)}_j = \lambda^{(k)}(\boldsymbol{r};t,t_0)\,W_{ij}(\boldsymbol{r},t_0)\,\phi(\boldsymbol{r})^{(k)}_j,$$
$$i,j,k=0,1. \tag{18}$$

Here, we have used two levels of ''fuzzing'' thus giving a 2×2 eigenvalue equation. We used level 0 (unfuzzed) and level 16, which means 16 transformations of the spatial links. The link/staple weighting used was 2.5. This choice of fuzzing parameters was made so as to give a satisfactory variational basis with a modest amount of computational effort. Initial tuning experiments were made using 20 configurations at $(\beta,\kappa^{\rm sea})=(5.2,0.135\,00)$ and repeated on a corresponding matched ensemble of quenched configurations. Expanding the basis to three levels of fuzzing did not significantly improve the resulting effective-mass plateaus extracted as described below.

In principle, one could use the largest eigenvalue $\lambda^{(0)}(\boldsymbol{r};t,t_0)$ for large t,t_0 to estimate the potential. In practice, however, the eigenvalue system becomes unstable at large t, particularly when modest numbers of configurations are used, as is often the case in dynamical fermion studies. Instead, we used the leading eigenvector $\phi(\boldsymbol{r})^{(0)}$, corresponding to $\lambda^{(0)}(\boldsymbol{r};t,t_0)$ at $t=1,t_0=0$, to project onto the approximate ground state [9,26]. The resulting correlator $\widetilde{W}_0(t)$ was then used to form effective-mass estimates for the approximate ground state,

$$\widetilde{E}_0(\boldsymbol{r},t) = \ln\left(\frac{\widetilde{W}_0(\boldsymbol{r},t)}{\widetilde{W}_0(\boldsymbol{r},t+1)}\right). \tag{19}$$

The ratio of the first two transfer-matrix eigenvalues,

$$R_{1,0} = \lambda^{(1)}(\boldsymbol{r};1,0)/\lambda^{(0)}(\boldsymbol{r};1,0), \tag{20}$$

was used to help obtain improved estimates of the ground-state energy with reduced contamination from the first excited state. To do this, the correlator $\widetilde{W}_0(t)$ was modelled as a sum of two exponential terms,

$$\widetilde{W}_0(\boldsymbol{r},t) \propto [\lambda^{(0)}(\boldsymbol{r};1,0)]^t + \epsilon_{1,0}[\lambda^{(1)}(\boldsymbol{r};1,0)]^t. \tag{21}$$

TABLE IV. The static potential $V(\boldsymbol{r})$ in lattice units. For the preliminary data at $\kappa^{\mathrm{sea}}=0.135\,65$, the configurations were measured every 10 trajectories and analyzed in bins of two.

	$(\beta,\kappa^{\mathrm{sea}})$					
$\boldsymbol{r}$	(5.20,0.1350)	(5.26,0.1345)	(5.29,0.1340)	(5.93,0)	(5.2,0.1355)	(5.2,0.13565)
(1,0,0)	0.4823(02)	0.4739(04)	0.4707(03)	0.4259(01)	0.4762(02)	0.4749(02)
(2,0,0)	0.6970(08)	0.6839(11)	0.6782(10)	0.6268(03)	0.6832(08)	0.6794(06)
(3,0,0)	0.8253(17)	0.8100(15)	0.8027(17)	0.7439(05)	0.7999(14)	0.7954(12)
(4,0,0)	0.9193(22)	0.9001(27)	0.8920(28)	0.8307(06)	0.8839(18)	0.8745(14)
(5,0,0)	0.9945(30)	0.9777(36)	0.9654(36)	0.9070(07)	0.9504(28)	0.939(02)
(6,0,0)	1.0628(43)	1.042(06)	1.0342(43)	0.9780(09)	1.0168(29)	1.002(02)
(7,0,0)	1.130(06)	1.105(06)	1.098(07)	1.0484(13)	1.0828(39)	1.061(04)
(8,0,0)	1.183(08)	1.175(09)	1.170(11)	1.1117(16)	1.135(05)	1.114(04)
(9,0,0)	1.262(11)	1.244(11)	1.244(11)	1.1802(26)	1.186(07)	1.165(05)
(10,0,0)	1.321(17)	1.285(21)	1.310(15)	1.243(4)	1.246(08)	1.221(07)
(11,0,0)	1.398(21)	1.414(23)	1.367(16)	1.301(5)	1.298(10)	1.277(11)
(12,0,0)	1.467(24)			1.365(8)	1.330(17)	1.287(25)
(1,1,0)	0.6276(05)	0.6156(06)	0.6103(07)	0.5514(2)	0.6173(05)	0.6140(04)
(2,1,0)	0.7495(09)	0.7315(13)	0.7288(11)	0.6671(4)	0.7310(09)	0.7262(07)
(2,2,0)	0.8163(14)	0.8001(17)	0.7940(15)	0.7319(5)	0.7944(10)	0.7884(10)
(3,1,0)	0.8483(15)	0.8296(16)	0.8226(16)	0.7616(6)	0.8215(15)	0.8138(11)
(3,2,0)	0.8873(18)	0.8687(27)	0.8636(23)	0.8009(7)	0.8599(15)	0.8497(14)
(3,3,0)	0.9387(24)	0.9235(26)	0.9122(22)	0.8517(9)	0.9051(17)	0.8939(18)
No. of Conf.	150	101	101	623	208	244
traj. spac.	40	40	40		40	10×2

One can easily show that, provided the contamination from the first excited state ($\epsilon_{1,0}$) is small, the true ground-state energy in such a model is given by

$$E_0(\boldsymbol{r})=-\ln\lambda^{(0)}(R_{1,0})\approx\frac{\tilde{E}_0(\boldsymbol{r},t)-R_{1,0}\tilde{E}_0(\boldsymbol{r},t-1)}{1-R_{1,0}}. \tag{22}$$

Rather than search for plateaus in this quantity, we used a weighted mean of values from t_{min} to t_{max} where the weighting was inversely proportional to the statistical error (estimated via simple jackknife). To obtain the final quoted values, we used $(t_{\mathrm{min}},t_{\mathrm{max}})=(4,5)$. In all cases, the difference due to increasing or decreasing the cutoffs by 1 was less than the statistical errors quoted. Overall statistical errors were estimated by bootstrap sampling.

We also studied double exponential fits to the effective mass $\tilde{E}_0(\boldsymbol{r},t)$ using time slices up to $t=8$ and exponential fits to the full 2×2 matrix correlator. The fits, where stable, yielded results compatible with those obtained by the above methods.

In Fig. 1, we show examples of the effective mass and corresponding extrapolated energy (22) used to determine $V(\boldsymbol{r})$. The lattice potential values are collected in Table IV.

B. Determination of r_0/a

The potential $V(\boldsymbol{r})$ can be used to determine the force between a static quark-antiquark pair separated by a distance $r=|\boldsymbol{r}|$ and hence to extract the Sommer scale parameter r_0. This is a characteristic scale at which one may match the interquark force with phenomenological potential models de-

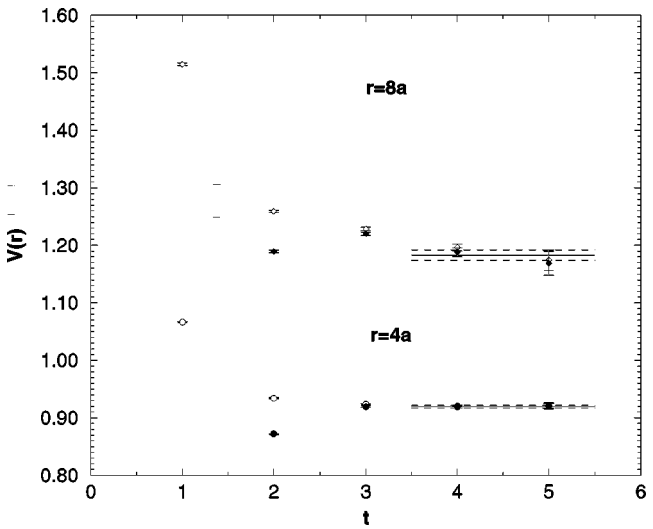

FIG. 1. Effective potential energies as a function of Euclidean time t (open symbols). The asymptotic estimates described in the text are shown as full symbols. The final estimated potential $V(r)$ is indicated by the lines with error bands. The data correspond to $(\beta,\kappa^{\mathrm{sea}})=(5.20,0.1350)$ and $\boldsymbol{r}=(4a,0,0)$ (circles) and $\boldsymbol{r}=(8a,0,0)$ (diamonds).

TABLE V. Sommer scale r_0 and other parameters deduced from the lattice potential.

$(\beta,\kappa^{\rm sea})$	r_0/a	a (fm)	e	$\sqrt{\sigma}$ (MeV)
(5.2,0.13565)	5.21(05)(+0−8)	0.0941(8)(+13−0)	0.315(7)(+18−11)	465(1)(+19−3)
(5.2,0.13550)	5.041(40)(+0−10)	0.0972(8)(+7−0)	0.307(6)(+17−1)	467(1)(+17−3)
(5.20,0.1350)	4.754(40)(+2−90)	0.1031(09)(+20−1)	0.326(07)(+32−12)	463(2)(+2−6)
(5.26,0.1345)	4.708(52)(+45−50)	0.1041(12)(+11−10)	0.298(09)(+100−8)	468(2)(+2−18)
(5.29,0.1340)	4.813(45)(+35−84)	0.1018(10)(+20−7)	0.310(10)(+0−61)	466(2)(+10−0)
(5.93,0)	4.714(13)(+0−18)	0.1040(03)(+4−0)	0.276(03)(+17−2)	471(1)(+21−3)

scribing quarkonia [9]. Specifically, it is defined by the solution of the relation

$$r_0^2 \left.\frac{dV}{dr}\right|_{r_0} = 1.65. \tag{23}$$

Physically, $r_0 \simeq 0.49$ fm, and we adopt this latter value when physical units are required. This definition of the physical scale has the advantage that one needs to know the potential only at intermediate distances. An extrapolation of the potential to large separation, which is conventionally performed to extract the string tension, is thus avoided. Hence, the procedure is well suited to the case of full QCD for which the definition of a string tension, as the limiting value of the force, is not applicable. The string is, of course, expected to break at some characteristic distance r_b.

Our determination of r_0/a follows the procedures originally described in [27] and recently adapted to provide a comprehensive study of the scale parameter in quenched QCD [22]. That is, we perform fits to the parametrization,

$$V(\boldsymbol{r}) = V_0 + \sigma r - e\left[\frac{1}{\boldsymbol{r}}\right] + f\left(\left[\frac{1}{\boldsymbol{r}}\right] - \frac{1}{r}\right), \tag{24}$$

where $[1/\boldsymbol{r}]$ is the tree-level lattice Coulomb term

$$\left[\frac{1}{\boldsymbol{r}}\right] = 4\pi \int_{-\pi}^{\pi} \frac{d^3k}{(2\pi)^3} \frac{\cos(\boldsymbol{k}\cdot\boldsymbol{r})}{4\sum_{j=1}^{3} \sin^2(k_j/2)}. \tag{25}$$

The parameter f is introduced so as to model further lattice corrections beyond tree level. We find that, for the coarse lattice spacings considered in this work, a tree-level parametrization gives a poor description of the data for $r \ll r_0$.

Following [22], we use fits of the form (24) to provide a good description of the intermediate range potential. We then identify the fitted parameters as reliable estimates [up to $O(a^2)$] of the corresponding continuum version which, from the definition of r_0, satisfies

$$\sigma r_0^2 + e = c \equiv 1.65 \tag{26}$$

and hence we extract our estimate of r_0 as

$$r_0 = \sqrt{\frac{c-e}{\sigma}}. \tag{27}$$

Both on- and off-axis measurements of the potential were used (see Table IV). We confirm the observation [22] that the value of r_0 extracted in this way is remarkably insensitive to changes in the fit range used. The individual parameters such as e and f are, however, quite sensitive. The point at $\boldsymbol{r} = (a,0,0)$ was omitted from all fits since its inclusion was found to give an unacceptably high contribution to χ^2. The inclusion of data at the largest $|\boldsymbol{r}|$ $(>8a)$ played little role in the determination of r_0. Since a limited range of $\boldsymbol{r}$ is used to determine the parameters of Eq. (24), one should treat the value of σ with some caution. It does not represent a careful determination of the string tension, which of course is a large distance property and, strictly speaking, only meaningful in the heavy sea-quark limit.

We present a summary of the results for r_0 in Table V. The systematic error estimates [shown as $(+x-y)$] were determined by variations in the fitting range used for $\boldsymbol{r}$ and in the number of parameters used in the fit. The central values quoted were obtained using all potential data satisfying $\sqrt{2} \leqslant \boldsymbol{r} \leqslant 8$. As described in the next subsection, a term proportional to $1/r^2$ was tried. The systematic error estimates also include the effects of varying $t_{\rm min}$ by one unit in the evaluation of the potential (see above). It is seen that, for the ensembles at (5.20,0.1350), (5.26,0.1345), and (5.93,0), the matching in $\hat{r}_0$ (and hence in effective lattice spacing) is very good (well within statistical errors) while that at (5.29,0.1340) is only slightly off (just over one standard deviation). The unmatched simulation at the lightest quark mass has a significantly smaller lattice spacing (seven standard deviations).

It is worth noting (Table IV) that the absolute values of the potential are not matched even when r_0 is. The same is true for the average plaquette and the generalized Wilson loops themselves, which go into the potential determination. All of these loop operators have large ultraviolet-sensitive contributions. In Sec. V, we will comment further on the extent to which matching is observed in other physical quantities.

The value $\hat{r}_0 = 4.714(13)$ for the quenched measurements at $\beta = 5.93$ may be compared to previous high statistics measurements in quenched simulations. The interpolating parametrizations of [22] and [28], respectively, suggest 4.757 and 4.741(18), in fair agreement with, but slightly larger than, our determination of this quantity at this particular value of β. The slight discrepancy of our result with that of Ref. [27] amounts to about one standard deviation.

The JLQCD Collaboration has presented preliminary re-

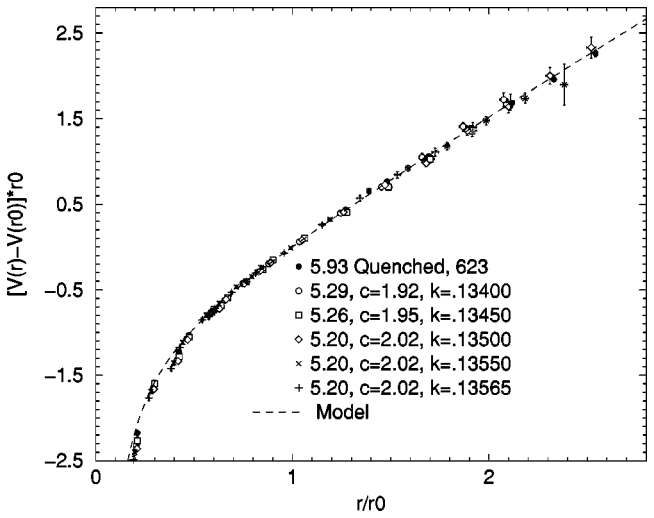

FIG. 2. The static QCD potential expressed in units of r_0. The dashed curve is a string model described in the text.

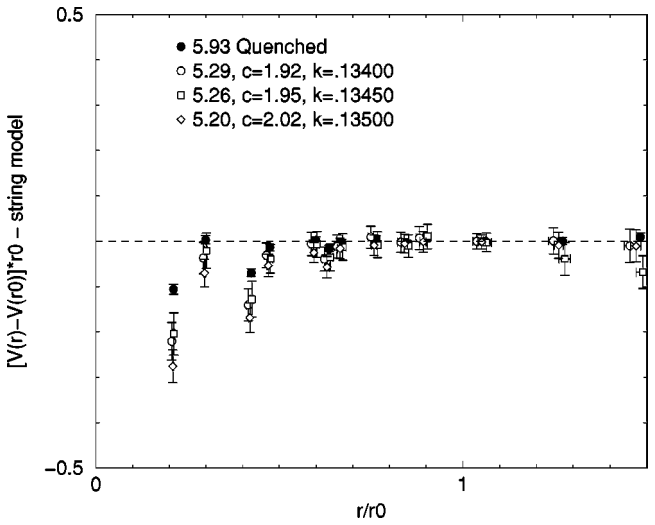

FIG. 3. The difference between the static QCD potential expressed in physical units and the prediction of the string model described in the text. For clarity, only data from the matched ensembles are shown.

sults from an $N_f=2$ simulation using the same action as the present work at $\beta=5.2$, $c_{\rm SW}=2.02$, and $\kappa=0.1350,0.1355$ [29]. The values of $\hat{r}_0$ in this case are slightly smaller than those presented in Table V. Note that the value of $c_{\rm SW}$ used by JLQCD is very slightly different from ours. The methods used to extract the potential and $\hat{r}_0$ apparently have much in common with those described above, but we have not been able to check all the details. In particular, the errors so far presented by JLQCD are statistical only.

As mentioned above, we have used both on-axis and off-axis Wilson loops in our determination of $\hat{r}_0$. However, different spatial orientations of Wilson loops differ by lattice artifacts of order a^2. Thus, if on-axis loops are used exclusively to extract $\hat{r}_0$, then the result may not be consistent with a determination using other orientations, provided that the statistical accuracy is large enough to expose these discrepancies. For our $N_f=2$ simulations, the level of precision is about 1%, so that any significant discrepancy in $\hat{r}_0$ due to different orientations will be hard to detect. In future high-statistics simulations with dynamical quarks, a cleaner procedure might be to define $\hat{r}_0$ consistently for one particular orientation and to extract $\hat{r}_0$ from local interpolations of the force between static quarks. This is the approach used in Refs. [9,25,27,8]. It has also been used for some of the ensembles presented here, and for r_0 itself it makes little difference (within the statistical errors).

C. Charge screening

In Fig. 2, we plot the static potential in units of r_0. The zero of the potential has been set at $r=r_0$. Overall, the presence of dynamical fermions makes little difference when plotted in physical units. The data are apparently well described by the universal bosonic string model potential [30], which predicts

$$[V(r)-V(r_0)]r_0=(1.65-e)\left(\frac{r}{r_0}-1\right)-e\left(\frac{r_0}{r}-1\right). \tag{28}$$

Of course, the fact that the scaled potential measurements all have the same value and slope at $r=r_0$ simply reflects the definition of r_0. In Fig. 3, we show the deviations from this model potential. Here $e=\pi/12$ [30]. We note the following points: (i) At the shortest distances (see the points where $|\boldsymbol{r}|<0.5r_0$) there are indeed deviations from the string model; (ii) the large fluctuations as a function of $\boldsymbol{r}/r_0$ indicate strong violations of rotational symmetry (see Table IV for a list of separations used); (iii) there is some slight evidence that the deviations depend systematically on the quark mass—compare the quenched points with those for the lightest values of $\kappa^{\rm sea}$; (iv) the matching of the data ensembles allows a clean comparison of the data at different quark masses; and (v) there are no indications of string breaking, but we note that the distance probed at light quarks masses is not large ($\boldsymbol{r}<1.3$ fm at the lightest quark masses used).

As discussed above, the parametrization (24) is not particularly efficient at describing the short-range interactions on the lattice. This is the case even though it allows, in a model-dependent way ($f\neq 0$), for lattice artifacts beyond those expected at tree level. The fits for the effective charge e and associated parameter f are therefore sensitive to the fit range and any variation in the parametrization. For example, we also considered allowing a term proportional to $|\boldsymbol{r}|^{-2}$ in an attempt to describe better the short distance potential. However, the coarseness of the lattice and crudeness of the parametrization prevented reliable fits. In the continuum limit, one would expect the short-range potential to behave as

$$V(\boldsymbol{r})=-\frac{4}{3}\frac{\alpha_s(\mu)}{|\boldsymbol{r}|}, \tag{29}$$

where μ is some scale. Lowest-order perturbation theory then suggests an enhancement of some 14% in α_s arising from the change in the factor $33-2N_f$ when unquenching the theory (at fixed scale). Using the above parametrization

(24), we can see if such an effect is reflected in a corresponding increase of 18% in the parameter e.

We have performed correlated fits to the potential with a constant choice of parametrization and fit ranges. Some reasonable variation in the latter was then used to give an estimate of systematic errors. The fits for the central values of parameters included all data from Table IV satisfying $\sqrt{2} \leqslant |\boldsymbol{r}|/a \leqslant 9$. The statistical errors were produced via an overall bootstrap of the full analysis (with 500 bootstrap samples). The results are included in Table V. The coupling parameter e does seem to show an increase due to unquenching. For the matched ensembles, the increase is $18^{+13}_{-10}\%$ in going from quenched to $\kappa^{\rm sea}=0.135\,00$.

Similar findings in the case of two flavors of Wilson fermions have been reported by the SESAM-TχL Collaboration [31], where an increase of 16–33 % was found.

For comparison with other scale determinations, we have included the fit parameter $\sqrt{\sigma}$ expressed in units of MeV as deduced from $r_0=0.49$ fm. We repeat the caveat offered above that the parameter $\sqrt{\sigma}$ reflects the medium-range shape of the potential and does not represent a definitive determination of the asymptotic string tension. Phenomenological models for the hadronic string suggest a value of around 440 MeV. The energy scale determination based on r_0/a is therefore some 6–7 % higher than that based on the string tension. In the next section we compare the above scale determination with values deduced from the vector meson mass.

Recently, the MILC Collaboration [32,33] has presented results of a comparison of the quenched static potential with that due to three flavors of staggered fermions. As in the present analysis, the authors have noted the strong influence of the dynamical quarks on the effective lattice spacing and have compared the shapes of the potential measured on matched ensembles.

V. LIGHT HADRON SPECTRUM

Throughout this section, one of our main aims will be to uncover any unquenching effects in the light hadron spectrum. Because we have a *matched* data set, any differences can more directly be attributed to unquenching effects. However, the task of identifying differences is likely to be hard for those quantities which are primarily sensitive to physics at the same scale as that used to define the matching trajectory in the $(\beta,\kappa^{\rm sea})$ parameter space (r_0 in this case). This is expected to be the case for the hadron spectrum considered here where the quark masses are still relatively heavy.

Two-point hadronic correlation functions were produced for each of the datasets appearing in Table I. The interpolating operators for pseudoscalar, vector, nucleon, and delta channels were those described in [34]. Mesonic correlators were constructed using both degenerate and nondegenerate valence quarks, whereas only degenerate valence quarks were used for the baryonic correlators.

The hadronic masses are presented in Tables VI–IX. These are expressed in both lattice units ($\hat{M}\equiv Ma$) and in the dimensionless form r_0M. Note that the errors displayed are statistical only. We estimate that the systematic errors arising from different choices of fitting procedure are similar in size to the statistical errors.

In the following, we review the main fitting procedures which were used to obtain the light hadron spectrum results. Further details of the fitting procedure can be found in [35].

A. Fitting procedure

We used the fuzzing procedures of [36] to generate correlators of the type LL, FL, and FF, where F denotes fuzzed and L is local operators. Conforming to our usual convention, FL means fuzzed at the source and local at the sink. The fuzzing radius was set to $R_{\rm fuzz}=2$.

Effective-mass plots for the three types of fuzzed correlators (LL, FL, and FF) are shown in Fig. 4 for the $\beta=5.2, \kappa^{\rm sea}=\kappa^{\rm val}=0.135\,00$ dataset. Note that all the effective-mass plots approach their asymptote from above. The FF correlator exhibits the fastest approach. This behavior is universal throughout all the datasets. For technical reasons, the fuzzing procedures used in practice for the hadron correlators introduced some unbiased stochastic noise. We have checked that this has indeed had no significant effect on the hadronic quantities presented here but has resulted in increased error estimates at the level of less than 10% for the pion and less than 20% for the nucleon.

Correlated fits were used throughout the fitting analysis of the correlation functions, and the eigenvalue smoothing technique of [37] was employed. Ensembles of 500 bootstrap samples were used to estimate the errors [38].

We performed a *factorizing fit* which we now describe for the baryonic case. The three fuzzed correlators LL, FL, and FF are fitted together, where the fitting function used for, say, the FL channel is

$$Z_0^{\rm L}Z_0^{\rm F}e^{-m_0t}+Z_1^{\rm L}Z_1^{\rm F}e^{-m_1t},$$

and the LL and FF fitting functions are similarly defined (see, e.g., [39]). Note that both the coefficients $Z_{0,1}$ and the masses $m_{0,1}$ are common to all the channels, and that the χ^2 comprises the individual χ^2 of the three channels and includes the correlation between different times and channels.

For the mesonic case, we modify the above as usual by including the backward-propagating state, i.e., $e^{-mt} \rightarrow e^{-m(T-t)}$, where T is the temporal extent of the lattice.

Within these three different fitting types, a *sliding window* analysis was used to determine the optimal fitting range $(t_{\rm min}-t_{\rm max})$ [40]. In this analysis, fits for various $t_{\rm min}$ were obtained with $t_{\rm max}$ fixed generally to 15. Stability requirements in the baryonic sector forced $t_{\rm max}=14$ in some cases. The masses so obtained are displayed in Tables VI–IX.

B. PCAC mass

The PCAC (partial conservation of axial vector current) mass can be defined using the relation

$$\partial_\mu A_\mu(x)=2m_{\rm PCAC}P(x),$$

where $P(x)$ and $A(x)$ are pseudoscalar and axial current densities. On the lattice, the following expression can be used to obtain an estimate of $m_{\rm PCAC}$ [41]:

TABLE VI. Pseudoscalar meson masses for all datasets.

β	$\kappa^{\rm sea}$	$\kappa_a^{\rm val}$	$\kappa_b^{\rm val}$	$r_0 M_{\rm PS}$	$aM_{\rm PS}$
5.2000	0.1355	0.1340	0.1340	2.39^{+3}_{-2}	0.473^{+2}_{-2}
5.2000	0.1355	0.1345	0.1340	2.25^{+3}_{-2}	0.447^{+2}_{-2}
5.2000	0.1355	0.1345	0.1345	2.12^{+3}_{-2}	0.420^{+2}_{-2}
5.2000	0.1355	0.1350	0.1340	2.12^{+3}_{-2}	0.420^{+2}_{-2}
5.2000	0.1355	0.1350	0.1345	1.97^{+3}_{-2}	0.391^{+3}_{-2}
5.2000	0.1355	0.1350	0.1350	1.82^{+3}_{-1}	0.362^{+3}_{-3}
5.2000	0.1355	0.1355	0.1340	1.98^{+3}_{-1}	0.392^{+3}_{-2}
5.2000	0.1355	0.1355	0.1345	1.82^{+3}_{-1}	0.362^{+3}_{-3}
5.2000	0.1355	0.1355	0.1350	1.66^{+3}_{-1}	0.329^{+3}_{-3}
5.2000	0.1355	0.1355	0.1355	1.48^{+3}_{-2}	0.294^{+4}_{-3}
5.2000	0.1350	0.1335	0.1335	2.68^{+2}_{-3}	0.563^{+3}_{-3}
5.2000	0.1350	0.1340	0.1335	2.56^{+2}_{-3}	0.539^{+3}_{-4}
5.2000	0.1350	0.1340	0.1340	2.45^{+2}_{-3}	0.514^{+3}_{-4}
5.2000	0.1350	0.1345	0.1335	2.44^{+2}_{-3}	0.514^{+3}_{-4}
5.2000	0.1350	0.1345	0.1340	2.32^{+2}_{-3}	0.489^{+3}_{-4}
5.2000	0.1350	0.1345	0.1345	2.20^{+2}_{-3}	0.462^{+4}_{-5}
5.2000	0.1350	0.1350	0.1335	2.32^{+2}_{-3}	0.488^{+3}_{-4}
5.2000	0.1350	0.1350	0.1340	2.20^{+2}_{-3}	0.462^{+4}_{-5}
5.2000	0.1350	0.1350	0.1345	2.06^{+2}_{-3}	0.434^{+4}_{-5}
5.2000	0.1350	0.1350	0.1350	1.93^{+2}_{-3}	0.405^{+4}_{-5}
5.2600	0.1345	0.1335	0.1335	2.85^{+2}_{-4}	0.603^{+2}_{-2}
5.2600	0.1345	0.1340	0.1335	2.74^{+2}_{-4}	0.580^{+2}_{-2}
5.2600	0.1345	0.1340	0.1340	2.63^{+2}_{-4}	0.557^{+2}_{-2}
5.2600	0.1345	0.1345	0.1335	2.63^{+2}_{-4}	0.557^{+2}_{-2}
5.2600	0.1345	0.1345	0.1340	2.52^{+2}_{-4}	0.533^{+2}_{-2}
5.2600	0.1345	0.1345	0.1345	2.41^{+2}_{-4}	0.509^{+2}_{-2}
5.2600	0.1345	0.1350	0.1335	2.52^{+2}_{-4}	0.533^{+2}_{-2}
5.2600	0.1345	0.1350	0.1340	2.41^{+2}_{-4}	0.509^{+2}_{-2}
5.2600	0.1345	0.1350	0.1345	2.29^{+2}_{-4}	0.484^{+2}_{-2}
5.2600	0.1345	0.1350	0.1350	2.16^{+2}_{-3}	0.458^{+2}_{-2}
5.2900	0.1340	0.1335	0.1335	2.99^{+2}_{-4}	0.621^{+2}_{-2}
5.2900	0.1340	0.1340	0.1335	2.88^{+2}_{-4}	0.599^{+2}_{-2}
5.2900	0.1340	0.1340	0.1340	2.78^{+2}_{-4}	0.577^{+2}_{-2}
5.2900	0.1340	0.1345	0.1335	2.78^{+2}_{-4}	0.577^{+2}_{-2}
5.2900	0.1340	0.1345	0.1340	2.67^{+2}_{-4}	0.554^{+2}_{-2}
5.2900	0.1340	0.1345	0.1345	2.55^{+2}_{-4}	0.530^{+2}_{-3}
5.2900	0.1340	0.1350	0.1335	2.67^{+2}_{-4}	0.554^{+2}_{-2}
5.2900	0.1340	0.1350	0.1340	2.55^{+2}_{-4}	0.530^{+2}_{-3}
5.2900	0.1340	0.1350	0.1345	2.43^{+2}_{-4}	0.506^{+2}_{-3}
5.2900	0.1340	0.1350	0.1350	2.31^{+2}_{-3}	0.480^{+3}_{-3}
5.9300	0.0000	0.1327	0.1327	2.334^{+6}_{-10}	0.495^{+1}_{-1}
5.9300	0.0000	0.1332	0.1327	2.211^{+6}_{-9}	0.469^{+1}_{-1}
5.9300	0.0000	0.1332	0.1332	2.081^{+6}_{-9}	0.442^{+1}_{-1}
5.9300	0.0000	0.1334	0.1327	2.159^{+6}_{-9}	0.458^{+1}_{-1}
5.9300	0.0000	0.1334	0.1332	2.028^{+6}_{-9}	0.430^{+1}_{-1}
5.9300	0.0000	0.1334	0.1334	1.973^{+6}_{-9}	0.419^{+1}_{-1}
5.9300	0.0000	0.1337	0.1337	1.800^{+6}_{-9}	0.382^{+1}_{-1}
5.9300	0.0000	0.1339	0.1337	1.739^{+6}_{-9}	0.369^{+1}_{-1}
5.9300	0.0000	0.1339	0.1339	1.676^{+6}_{-9}	0.356^{+1}_{-1}

TABLE VII. Vector meson masses for all datasets.

β	$\kappa^{\rm sea}$	$\kappa_a^{\rm val}$	$\kappa_b^{\rm val}$	$r_0 M_V$	aM_V
5.2000	0.1355	0.1340	0.1340	3.01^{+5}_{-2}	0.596^{+6}_{-2}
5.2000	0.1355	0.1345	0.1340	2.92^{+5}_{-3}	0.578^{+6}_{-6}
5.2000	0.1355	0.1345	0.1345	2.82^{+5}_{-3}	0.560^{+7}_{-6}
5.2000	0.1355	0.1350	0.1340	2.84^{+5}_{-3}	0.563^{+7}_{-6}
5.2000	0.1355	0.1350	0.1345	2.75^{+6}_{-3}	0.546^{+8}_{-7}
5.2000	0.1355	1350	0.1350	2.68^{+7}_{-4}	0.531^{+10}_{-8}
5.2000	0.1355	0.1355	0.1340	2.79^{+6}_{-4}	0.553^{+10}_{-8}
5.2000	0.1355	0.1355	0.1345	2.71^{+7}_{-4}	0.537^{+11}_{-9}
5.2000	0.1355	0.1355	0.1350	2.63^{+8}_{-5}	0.522^{+13}_{-9}
5.2000	0.1355	0.1355	0.1355	2.56^{+10}_{-4}	0.508^{+18}_{-10}
5.2000	0.1350	0.1335	0.1335	3.31^{+3}_{-4}	0.695^{+4}_{-4}
5.2000	0.1350	0.1340	0.1335	3.22^{+3}_{-4}	0.677^{+4}_{-5}
5.2000	0.1350	0.1340	0.1340	3.13^{+3}_{-4}	0.658^{+5}_{-5}
5.2000	0.1350	0.1345	0.1335	3.13^{+3}_{-4}	0.658^{+5}_{-5}
5.2000	0.1350	0.1345	0.1340	3.04^{+3}_{-4}	0.638^{+5}_{-6}
5.2000	0.1350	0.1345	0.1345	2.94^{+3}_{-4}	0.619^{+6}_{-7}
5.2000	0.1350	0.1350	0.1335	3.03^{+3}_{-4}	0.638^{+5}_{-5}
5.2000	0.1350	0.1350	0.1340	2.94^{+3}_{-4}	0.618^{+6}_{-6}
5.2000	0.1350	0.1350	0.1345	2.85^{+3}_{-5}	0.599^{+6}_{-7}
5.2000	0.1350	0.1350	0.1350	2.75^{+4}_{-5}	0.579^{+7}_{-9}
5.2600	0.1345	0.1335	0.1335	3.41^{+3}_{-5}	0.721^{+4}_{-4}
5.2600	0.1345	0.1340	0.1335	3.32^{+3}_{-5}	0.703^{+4}_{-4}
5.2600	0.1345	0.1340	0.1340	3.24^{+3}_{-5}	0.685^{+4}_{-4}
5.2600	0.1345	0.1345	0.1335	3.24^{+3}_{-5}	0.685^{+4}_{-4}
5.2600	0.1345	0.1345	0.1340	3.16^{+3}_{-5}	0.668^{+4}_{-4}
5.2600	0.1345	0.1345	0.1345	3.07^{+3}_{-5}	0.650^{+4}_{-4}
5.2600	0.1345	0.1350	0.1335	3.16^{+3}_{-5}	0.668^{+4}_{-5}
5.2600	0.1345	0.1350	0.1340	3.08^{+3}_{-5}	0.651^{+4}_{-5}
5.2600	0.1345	0.1350	0.1345	2.99^{+3}_{-5}	0.633^{+5}_{-5}
5.2600	0.1345	0.1350	0.1350	2.91^{+3}_{-5}	0.614^{+5}_{-5}
5.2900	0.1340	0.1335	0.1335	3.49^{+3}_{-6}	0.725^{+5}_{-5}
5.2900	0.1340	0.1340	0.1335	3.41^{+3}_{-6}	0.708^{+6}_{-6}
5.2900	0.1340	0.1340	0.1340	3.32^{+3}_{-6}	0.691^{+6}_{-6}
5.2900	0.1340	0.1345	0.1335	3.32^{+3}_{-6}	0.691^{+6}_{-6}
5.2900	0.1340	0.1345	0.1340	3.24^{+4}_{-6}	0.674^{+6}_{-6}
5.2900	0.1340	0.1345	0.1345	3.16^{+4}_{-6}	0.656^{+7}_{-7}
5.2900	0.1340	0.1350	0.1335	3.24^{+4}_{-6}	0.674^{+7}_{-7}
5.2900	0.1340	0.1350	0.1340	3.16^{+4}_{-6}	0.656^{+7}_{-7}
5.2900	0.1340	0.1350	0.1345	3.08^{+4}_{-6}	0.639^{+8}_{-8}
5.2900	0.1340	0.1350	0.1350	3.00^{+4}_{-6}	0.623^{+8}_{-8}
5.9300	0.0000	0.1327	0.1327	3.05^{+1}_{-2}	0.646^{+2}_{-3}
5.9300	0.0000	0.1332	0.1327	2.97^{+1}_{-2}	0.629^{+3}_{-3}
5.9300	0.0000	0.1332	0.1332	2.88^{+2}_{-2}	0.612^{+3}_{-3}
5.9300	0.0000	0.1334	0.1327	2.93^{+2}_{-2}	0.622^{+3}_{-3}
5.9300	0.0000	0.1334	0.1332	2.85^{+2}_{-2}	0.605^{+3}_{-3}
5.9300	0.0000	0.1334	0.1334	2.82^{+2}_{-2}	0.598^{+3}_{-4}
5.9300	0.0000	0.1337	0.1337	2.72^{+2}_{-2}	0.577^{+4}_{-4}
5.9300	0.0000	0.1339	0.1337	2.69^{+2}_{-2}	0.570^{+5}_{-4}
5.9300	0.0000	0.1339	0.1339	2.66^{+3}_{-3}	0.563^{+5}_{-5}

TABLE VIII. Nucleon masses for all datasets.

β	$\kappa^{\rm sea}$	$\kappa^{\rm val}$	$r_0 M_N$	aM_N
5.2000	0.1355	0.1340	4.75^{+9}_{-6}	0.942^{+12}_{-13}
5.2000	0.1355	0.1345	4.42^{+9}_{-6}	0.876^{+15}_{-15}
5.2000	0.1355	0.1350	4.09^{+10}_{-7}	0.81^{+2}_{-2}
5.2000	0.1355	0.1355	3.86^{+7}_{-5}	0.766^{+11}_{-11}
5.2000	0.1350	0.1335	5.16^{+5}_{-6}	1.086^{+8}_{-8}
5.2000	0.1350	0.1340	4.87^{+5}_{-6}	1.024^{+8}_{-9}
5.2000	0.1350	0.1345	4.54^{+5}_{-7}	0.954^{+8}_{-11}
5.2000	0.1350	0.1350	4.20^{+5}_{-7}	0.883^{+10}_{-12}
5.2600	0.1345	0.1335	5.32^{+5}_{-9}	1.125^{+8}_{-8}
5.2600	0.1345	0.1340	5.05^{+5}_{-9}	1.068^{+9}_{-8}
5.2600	0.1345	0.1345	4.78^{+5}_{-9}	1.011^{+10}_{-9}
5.2600	0.1345	0.1350	4.50^{+6}_{-9}	0.951^{+10}_{-10}
5.2900	0.1340	0.1335	5.50^{+5}_{-9}	1.143^{+8}_{-8}
5.2900	0.1340	0.1340	5.23^{+5}_{-8}	1.086^{+9}_{-9}
5.2900	0.1340	0.1345	4.94^{+6}_{-9}	1.027^{+10}_{-10}
5.2900	0.1340	0.1350	4.66^{+7}_{-9}	0.968^{+13}_{-12}
5.9300	0.0000	0.1327	4.56^{+2}_{-3}	0.968^{+5}_{-6}
5.9300	0.0000	0.1332	4.25^{+3}_{-4}	0.902^{+5}_{-8}
5.9300	0.0000	0.1334	4.13^{+3}_{-4}	0.876^{+6}_{-8}
5.9300	0.0000	0.1337	3.94^{+3}_{-5}	0.836^{+7}_{-9}
5.9300	0.0000	0.1339	3.86^{+4}_{-4}	0.818^{+7}_{-8}

TABLE IX. Delta masses for all datasets.

β	$\kappa^{\rm sea}$	$\kappa^{\rm val}$	$r_0 M_\Delta$	aM_Δ
5.2000	0.1355	0.1340	5.12^{+10}_{-5}	1.015^{+15}_{-12}
5.2000	0.1355	0.1345	4.87^{+10}_{-6}	0.967^{+17}_{-15}
5.2000	0.1355	0.1350	4.64^{+11}_{-7}	0.92^{+2}_{-2}
5.2000	0.1355	0.1355	4.30^{+15}_{-11}	0.85^{+3}_{-2}
5.2000	0.1350	0.1335	5.57^{+6}_{-8}	1.172^{+11}_{-11}
5.2000	0.1350	0.1340	5.31^{+6}_{-8}	1.116^{+11}_{-12}
5.2000	0.1350	0.1345	5.02^{+7}_{-8}	1.055^{+13}_{-15}
5.2000	0.1350	0.1350	4.75^{+8}_{-10}	1.00^{+2}_{-2}
5.2600	0.1345	0.1335	5.61^{+5}_{-9}	1.186^{+11}_{-10}
5.2600	0.1345	0.1340	5.36^{+5}_{-9}	1.134^{+11}_{-11}
5.2600	0.1345	0.1345	5.11^{+6}_{-9}	1.080^{+12}_{-11}
5.2600	0.1345	0.1350	4.83^{+7}_{-10}	1.022^{+14}_{-13}
5.2900	0.1340	0.1335	5.80^{+6}_{-10}	1.205^{+11}_{-10}
5.2900	0.1340	0.1340	5.56^{+6}_{-10}	1.155^{+12}_{-11}
5.2900	0.1340	0.1345	5.33^{+6}_{-10}	1.107^{+11}_{-13}
5.2900	0.1340	0.1350	5.09^{+7}_{-9}	1.057^{+13}_{-12}
5.9300	0.000	0.1327	5.09^{+3}_{-4}	1.079^{+7}_{-8}
5.9300	0.000	0.1332	4.84^{+4}_{-5}	1.026^{+8}_{-9}
5.9300	0.000	0.1334	4.74^{+4}_{-5}	1.005^{+9}_{-9}
5.9300	0.000	0.1337	4.58^{+5}_{-5}	0.972^{+11}_{-11}
5.9300	0.000	0.1339	4.47^{+6}_{-6}	0.949^{+12}_{-11}

$$m_{\rm PCAC} = \left\langle \frac{\tilde{\partial}_4 C_{A_4 P^\dagger}(\vec{0},t) + a c_A \partial_4^* \partial_4 C_{PP^\dagger}(\vec{0},t)}{2 C_{PP^\dagger}(\vec{0},t)} \right\rangle$$

$$= \langle r(t) \rangle + c_A \langle s(t) \rangle, \tag{30}$$

where $\tilde{\partial}_4$ is the temporal lattice derivative averaged over the forward, ∂, and backward, ∂^*, directions, and $\langle\,\rangle$ represents averaging over times, t, where the asymptotic state dominates. The correlators C are defined in [34]. The value of the coefficient used is

$$c_4 = -0.007\,56 g_0^2, \tag{31}$$

with $g_0^2 = 6/\beta$ (the bare coupling). This is the one-loop, dynamical value [42], and hence Eq. (30) suffers from $O(a)$ errors. Table X shows the results for $m_{\rm PCAC}$ for all the datasets with c_A defined as in Eq. (31).

There has been some recent debate in the literature regarding the most suitable nonperturbatively improved c_A value (see, e.g., [43–45]) and a reliable value may not yet have been determined. In the absence of a nonperturbatively improved value of c_A (for $N_f = 2$), we choose to display also in Table XI the values for $\langle r(t) \rangle$ and $\langle s(t) \rangle$. With these numbers, the reader can readily obtain the values for $m_{\rm PCAC}$ with any choice of c_A.

C. The J parameter

In Figs. 5 and 6, the vector meson masses and hyperfine splittings are plotted against the corresponding pseudoscalar masses for all the datasets. It is difficult to identify an unquenching signal from these plots, as the data seem to overlay each other. Note that in [8], it was reported that there was a tendency for the vector mass to *increase* as the sea quark mass *decreases* (for fixed pseudoscalar mass). The observations for the present *matched* dataset imply that this may have been due to either an $O(a)$ effect (since the dataset in [8] was not fully improved at this level) or a finite volume effect. The conclusion, therefore, is that it is important to run at a fixed a in order to disentangle unquenching effects from lattice artifacts or finite volume effects.

A possible explanation as to why there is no signal of unquenching in our meson spectrum is the following. Our matched ensembles are defined to have a common r_0 value, so any physical quantity that is sensitive to this distance scale (and the static quark potential itself) will also, by definition, be matched. Our mesons, because they are composed of relatively heavy quarks, are examples of such quantities, and this is a possible reason why there is no significant evidence of unquenching effects in the meson spectrum.

When comparing the experimental data points with the lattice data in Figs. 5 and 6, we note that the lattice data are high. This could be due to an incorrect value of r_0 being used ($r_0 = 0.49$ fm) and that the true value of r_0 is somewhat higher. This possibility is discussed again in the next section.

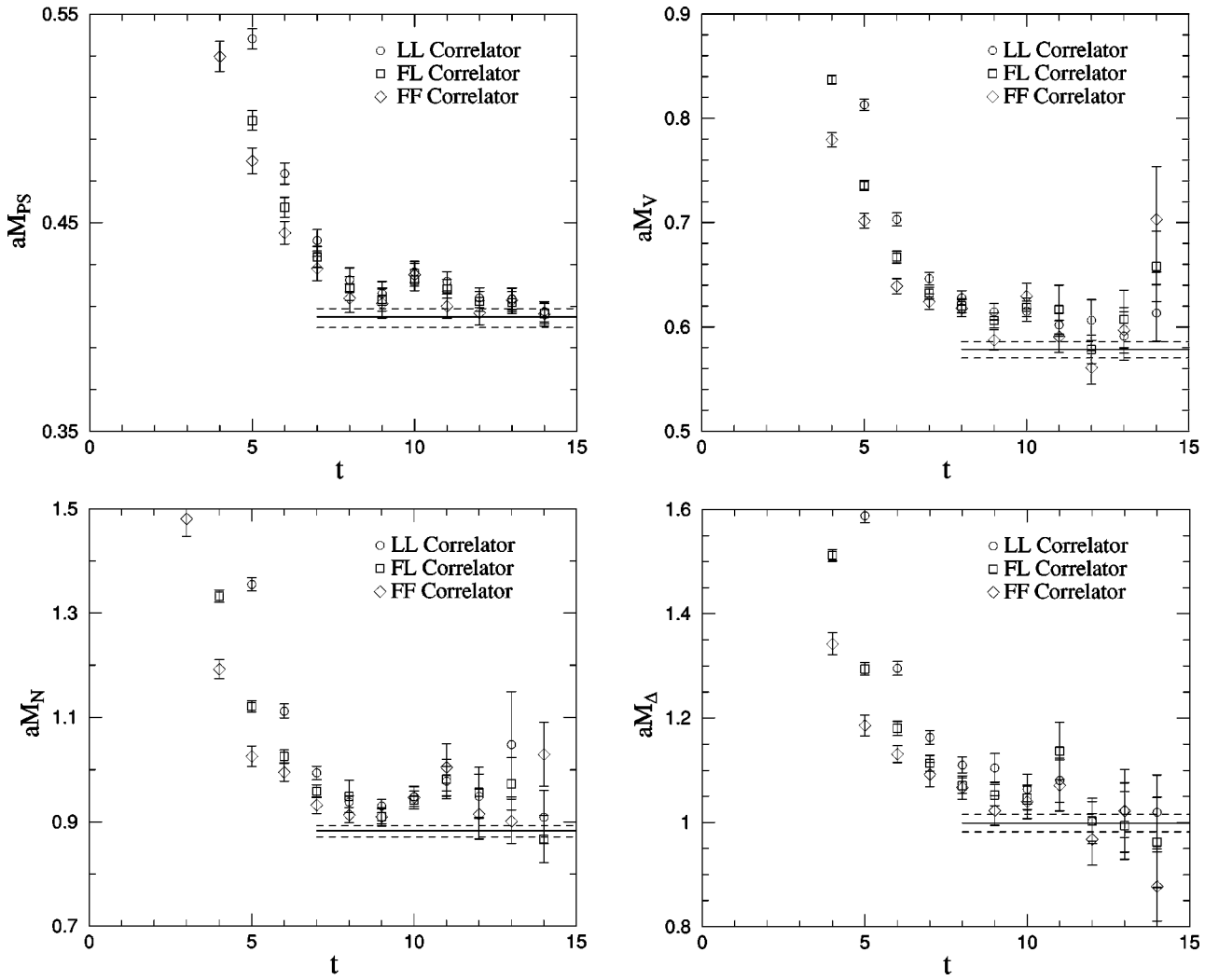

FIG. 4. Effective mass plots for the pseudoscalar, vector, nucleon, and delta for the $\beta=5.2$, $\kappa^{\mathrm{sea}}=0.135\,00$ data set at $\kappa^{\mathrm{val}}=0.135\,00$. The horizontal lines show the fitted value for the mass (with error bars) obtained by the fitting approach described in the text.

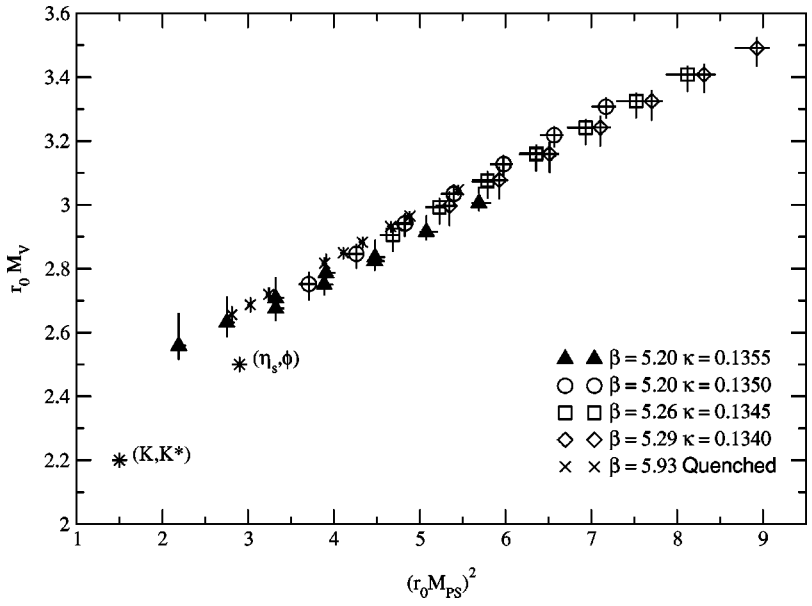

FIG. 5. Vector mass plotted against pseudoscalar mass squared in units of r_0, together with the experimental data points.

TABLE X. The quark mass m_{PCAC} as defined in Eq. (30) for all datasets.

β	κ^{sea}	κ_a^{val}	κ_b^{val}	$r_0 m_{\mathrm{PCAC}}$	$a m_{\mathrm{PCAC}}$
5.20	0.1355	0.1340	0.1340	0.329^{+4}_{-2}	0.0652^{+2}_{-3}
5.20	0.1355	0.1345	0.1340	0.292^{+3}_{-2}	0.0580^{+2}_{-3}
5.20	0.1355	0.1345	0.1345	0.256^{+3}_{-2}	0.0508^{+2}_{-2}
5.20	0.1355	0.1350	0.1340	0.256^{+3}_{-2}	0.0508^{+2}_{-3}
5.20	0.1355	0.1350	0.1345	0.221^{+3}_{-2}	0.0438^{+2}_{-3}
5.20	0.1355	0.1350	0.1350	0.185^{+3}_{-2}	0.0368^{+2}_{-3}
5.20	0.1355	0.1355	0.1340	0.221^{+3}_{-2}	0.0438^{+2}_{-3}
5.20	0.1355	0.1355	0.1345	0.186^{+3}_{-2}	0.0368^{+2}_{-3}
5.20	0.1355	0.1355	0.1350	0.151^{+2}_{-2}	0.0299^{+3}_{-3}
5.20	0.1355	0.1355	0.1355	0.116^{+2}_{-2}	0.0231^{+3}_{-3}
5.20	0.1350	0.1335	0.1335	0.424^{+3}_{-4}	0.093^{+2}_{-2}
5.20	0.1350	0.1340	0.1335	0.389^{+3}_{-4}	0.0819^{+2}_{-2}
5.20	0.1350	0.1340	0.1340	0.355^{+2}_{-4}	0.0746^{+2}_{-2}
5.20	0.1350	0.1345	0.1335	0.355^{+3}_{-4}	0.0746^{+2}_{-2}
5.20	0.1350	0.1345	0.1340	0.320^{+2}_{-3}	0.0674^{+2}_{-2}
5.20	0.1350	0.1345	0.1345	0.287^{+2}_{-3}	0.0602^{+2}_{-3}
5.20	0.1350	0.1350	0.1335	0.320^{+2}_{-3}	0.0674^{+2}_{-2}
5.20	0.1350	0.1350	0.1340	0.286^{+2}_{-3}	0.0602^{+2}_{-3}
5.20	0.1350	0.1350	0.1345	0.253^{+2}_{-3}	0.0532^{+2}_{-3}
5.20	0.1350	0.1350	0.1350	0.220^{+2}_{-2}	0.0462^{+2}_{-3}
5.26	0.1345	0.1335	0.1335	0.491^{+3}_{-8}	0.1038^{+3}_{-3}
5.26	0.1345	0.1340	0.1335	0.455^{+3}_{-7}	0.0963^{+3}_{-3}
5.26	0.1345	0.1340	0.1340	0.420^{+3}_{-6}	0.0888^{+3}_{-3}
5.26	0.1345	0.1345	0.1335	0.420^{+3}_{-6}	0.0888^{+3}_{-3}
5.26	0.1345	0.1345	0.1340	0.385^{+3}_{-6}	0.0815^{+3}_{-3}
5.26	0.1345	0.1345	0.1345	0.351^{+3}_{-6}	0.0742^{+3}_{-3}
5.26	0.1345	0.1350	0.1335	0.385^{+3}_{-6}	0.0814^{+3}_{-3}
5.26	0.1345	0.1350	0.1340	0.351^{+3}_{-6}	0.0742^{+3}_{-3}
5.26	0.1345	0.1350	0.1345	0.317^{+2}_{-5}	0.0670^{+3}_{-3}
5.26	0.1345	0.1350	0.1350	0.283^{+2}_{-5}	0.0599^{+3}_{-3}
5.29	0.1340	0.1335	0.1335	0.530^{+4}_{-7}	0.1101^{+3}_{-3}
5.29	0.1340	0.1340	0.1335	0.494^{+4}_{-7}	0.1026^{+3}_{-3}
5.29	0.1340	0.1340	0.1340	0.458^{+4}_{-6}	0.0952^{+3}_{-3}
5.29	0.1340	0.1345	0.1335	0.458^{+4}_{-6}	0.0951^{+3}_{-3}
5.29	0.1340	0.1345	0.1340	0.423^{+4}_{-6}	0.0878^{+3}_{-3}
5.29	0.1340	0.1345	0.1345	0.387^{+3}_{-5}	0.0805^{+3}_{-3}
5.29	0.1340	0.1350	0.1335	0.422^{+4}_{-6}	0.0877^{+3}_{-3}
5.29	0.1340	0.1350	0.1340	0.387^{+3}_{-5}	0.0805^{+3}_{-3}
5.29	0.1340	0.1350	0.1345	0.353^{+3}_{-5}	0.0733^{+3}_{-3}
5.29	0.1340	0.1350	0.1350	0.318^{+3}_{-5}	0.0661^{+3}_{-3}
5.93	0.0000	0.1327	0.1327	0.3530^{+10}_{-12}	0.07488^{+11}_{-11}
5.93	0.0000	0.1332	0.1327	0.3162^{+9}_{-11}	0.06709^{+11}_{-11}
5.93	0.0000	0.1332	0.1332	0.2799^{+8}_{-10}	0.05938^{+11}_{-11}
5.93	0.0000	0.1334	0.1327	0.3016^{+9}_{-11}	0.06398^{+11}_{-12}
5.93	0.0000	0.1334	0.1332	0.2653^{+8}_{-10}	0.05629^{+11}_{-12}
5.93	0.0000	0.1334	0.1334	0.2508^{+8}_{-10}	0.05322^{+12}_{-11}
5.93	0.0000	0.1337	0.1337	0.2077^{+7}_{-8}	0.04406^{+12}_{-11}
5.93	0.0000	0.1339	0.1337	0.1931^{+7}_{-8}	0.04097^{+12}_{-11}
5.93	0.0000	0.1339	0.1339	0.1786^{+7}_{-8}	0.3788^{+13}_{-12}

TABLE XI. The values of $\langle r(t) \rangle$ and $\langle s(t) \rangle$ used to define m_{PCAC}, see Eq. (30).

β	κ^{sea}	κ_a^{val}	κ_b^{val}	$r(t)$	$s(t)$
5.20	0.1355	0.1340	0.1340	0.0662^{+2}_{-3}	0.1179^{+9}_{-8}
5.20	0.1355	0.1345	0.1340	0.0589^{+2}_{-3}	0.1050^{+9}_{-8}
5.20	0.1355	0.1345	0.1345	0.0516^{+2}_{-3}	0.0923^{+9}_{-8}
5.20	0.1355	0.1350	0.1340	0.0516^{+2}_{-2}	0.0924^{+9}_{-8}
5.20	0.1355	0.1350	0.1345	0.0445^{+2}_{-3}	0.0799^{+10}_{-8}
5.20	0.1355	0.1350	0.1350	0.0374^{+2}_{-3}	0.0678^{+9}_{-8}
5.20	0.1355	0.1355	0.1340	0.0445^{+2}_{-3}	0.0801^{+9}_{-8}
5.20	0.1355	0.1355	0.1345	0.0374^{+2}_{-3}	0.0678^{+9}_{-8}
5.20	0.1355	0.1355	0.1350	0.0304^{+3}_{-3}	0.0558^{+9}_{-8}
5.20	0.1355	0.1355	0.1355	0.0235^{+3}_{-3}	0.0441^{+9}_{-7}
5.20	0.1350	0.1335	0.1335	0.0907^{+2}_{-2}	0.1682^{+11}_{-9}
5.20	0.1350	0.1340	0.1335	0.0832^{+2}_{-2}	0.1538^{+10}_{-9}
5.20	0.1350	0.1340	0.1340	0.0758^{+2}_{-2}	0.1397^{+10}_{-10}
5.20	0.1350	0.1345	0.1335	0.0758^{+3}_{-2}	0.1397^{+10}_{-10}
5.20	0.1350	0.1345	0.1340	0.0685^{+2}_{-3}	0.1258^{+10}_{-9}
5.20	0.1350	0.1345	0.1345	0.0612^{+2}_{-3}	0.1123^{+10}_{-9}
5.20	0.1350	0.1350	0.1335	0.0685^{+2}_{-3}	0.1260^{+10}_{-10}
5.20	0.1350	0.1350	0.1340	0.0612^{+2}_{-3}	0.1123^{+10}_{-10}
5.20	0.1350	0.1350	0.1345	0.0541^{+2}_{-3}	0.0990^{+10}_{-10}
5.20	0.1350	0.1350	0.1350	0.0469^{+2}_{-3}	0.0859^{+10}_{-9}
5.26	0.1345	0.1335	0.1335	0.1055^{+3}_{-3}	0.1924^{+11}_{-9}
5.26	0.1345	0.1340	0.1335	0.0978^{+3}_{-3}	0.1779^{+10}_{-9}
5.26	0.1345	0.1340	0.1340	0.0903^{+3}_{-3}	0.1636^{+10}_{-8}
5.26	0.1345	0.1345	0.1335	0.0902^{+3}_{-3}	0.1637^{+10}_{-8}
5.26	0.1345	0.1345	0.1340	0.0828^{+3}_{-3}	0.1496^{+9}_{-8}
5.26	0.1345	0.1345	0.1345	0.0754^{+3}_{-3}	0.1359^{+9}_{-8}
5.26	0.1345	0.1350	0.1335	0.0827^{+3}_{-3}	0.1498^{+10}_{-8}
5.26	0.1345	0.1350	0.1340	0.0753^{+3}_{-3}	0.1360^{+9}_{-8}
5.26	0.1345	0.1350	0.1345	0.0680^{+3}_{-3}	0.1225^{+9}_{-8}
5.26	0.1345	0.1350	0.1350	0.0608^{+3}_{-3}	0.1093^{+9}_{-8}
5.29	0.1340	0.1335	0.1335	0.1119^{+3}_{-3}	0.2005^{+12}_{-11}
5.29	0.1340	0.1340	0.1335	0.1042^{+3}_{-3}	0.1862^{+12}_{-12}
5.29	0.1340	0.1340	0.1340	0.0967^{+3}_{-3}	0.1721^{+12}_{-11}
5.29	0.1340	0.1345	0.1335	0.0966^{+3}_{-3}	0.1721^{+12}_{-12}
5.29	0.1340	0.1345	0.1340	0.0892^{+3}_{-3}	0.1583^{+12}_{-12}
5.29	0.1340	0.1345	0.1345	0.0818^{+3}_{-3}	0.1447^{+12}_{-11}
5.29	0.1340	0.1350	0.1335	0.0891^{+3}_{-3}	0.1583^{+12}_{-12}
5.29	0.1340	0.1350	0.1340	0.0817^{+3}_{-3}	0.1447^{+12}_{-12}
5.29	0.1340	0.1350	0.1345	0.0744^{+3}_{-3}	0.1314^{+12}_{-11}
5.29	0.1340	0.1350	0.1350	0.0671^{+3}_{-3}	0.1182^{+12}_{-11}
5.93	0.0000	0.1327	0.1327	0.07584^{+11}_{-12}	0.1260^{+4}_{-5}
5.93	0.0000	0.1332	0.1327	0.06795^{+12}_{-12}	0.1127^{+4}_{-5}
5.93	0.0000	0.1332	0.1332	0.06014^{+11}_{-12}	0.0997^{+4}_{-5}
5.93	0.0000	0.1334	0.1327	0.06480^{+11}_{-12}	0.1075^{+4}_{-5}
5.93	0.0000	0.1334	0.1332	0.05702^{+11}_{-12}	0.0945^{+4}_{-5}
5.93	0.0000	0.1334	0.1334	0.05390^{+12}_{-12}	0.0894^{+4}_{-5}
5.93	0.0000	0.1337	0.1337	0.04464^{+12}_{-11}	0.0754^{+4}_{-4}
5.93	0.0000	0.1339	0.1337	0.04151^{+12}_{-11}	0.0703^{+4}_{-4}
5.93	0.0000	0.1339	0.1339	0.03838^{+13}_{-12}	0.0653^{+4}_{-4}

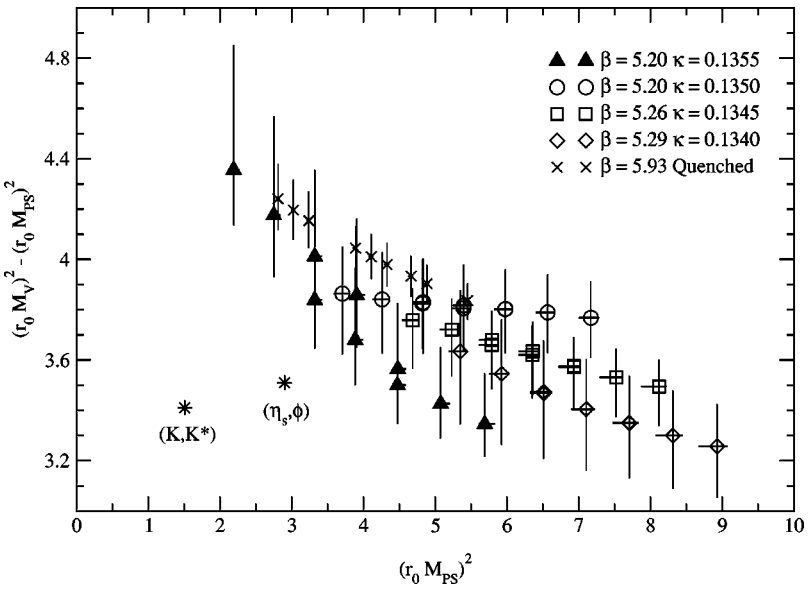

FIG. 6. Vector-pseudoscalar hyperfine splitting in units of r_0.

A further point regarding hyperfine splitting in Fig. 6 is that the lattice data for the *matched* ensembles tend to flatten as the sea quark mass decreases. (The quenched data have a distinctly negative slope, whereas the $\kappa^{\rm sea}=0.1350$ data are flat.) Thus the lattice data are tending toward the same behavior as the experimental data, which lie on a line with *positive* slope (independent of the value used for r_0). This behavior is apparently spoiled by the unmatched run with $\kappa^{\rm sea}=0.1355$ (see Fig. 6), which has a clear *negative* slope. However, the $\kappa^{\rm sea}=0.1355$ data do not satisfy the finite volume bound of [8] (see Sec. V E). One would expect that these finite volume effects would squeeze the vector meson state more than the pseudoscalar state (the ρ is an extended object). Furthermore, the more the valence quark mass was decreased, the more the vector mass would be raised by finite volume systematics. These considerations match with the observed behavior of the $\kappa^{\rm sea}=0.1355$ data in Fig. 6. The JLQCD Collaboration [29] has recently reported on a finite volume analysis with the same action as used in this work. For $\beta=5.2,\kappa^{\rm sea}=0.1350$, they found no evidence of finite-volume effects in their 16^3 data for either the pseudoscalar or vector meson. It would be interesting to extend this analysis to their $\beta=5.2,\kappa^{\rm sea}=0.1355$ dataset.

The J parameter is defined [46] as

$$J=M_V\left.\frac{dM_V}{dM_{\rm PS}^2}\right|_{K,K*}. \tag{32}$$

In the context of dynamical fermion simulations, this parameter can be calculated in two ways. The first is to define a partially quenched J for each value of the sea quark mass. In this case, the derivative in Eq. (32) is with respect to variations in the valence quark mass (with the sea quark mass fixed). The second approach is to define J along what we will term the "unitary" trajectory, i.e., along $\kappa^{\rm sea}=\kappa^{\rm val}$. In Table XII, the results from both methods are given. These values of J are around 25% lower than the experimental value[3] $J_{\rm expt}=0.48(2)$.

Finally, we note that the physical value of J [i.e., that which most closely follows the procedure used to determine the experimental value of $J_{\rm expt}=0.48(2)$] should be obtained from extrapolating the results from the first approach to the physical sea quark masses. We call this the third approach. In order to perform this extrapolation, we extrapolate the three matched dynamical J values obtained from the first approach linearly in $(M_{\rm PS}^{\rm unitary})^2$ to $(M_{\rm PS}^{\rm unitary})^2=0$. $M_{\rm PS}^{\rm unitary}$ is the pseudoscalar meson mass at the unitary point (i.e., where the valence and sea quark masses are all degenerate). The value for J from the third approach is presented in Table XII, and we note that it is approaching the experimental value for J.

The results from all three approaches are plotted in Fig. 7, together with the experimental result. There is some promising evidence that the lattice estimate of J increases toward

TABLE XII. J values from the various approaches as described in the text.

β	$\kappa^{\rm sea}$	J
	First approach	
5.2000	0.1355	0.32^{+2}_{-4}
5.2000	0.1350	0.393^{+10}_{-9}
5.2600	0.1345	0.365^{+6}_{-6}
5.2900	0.1340	0.349^{+7}_{-8}
5.9300	0.000	0.376^{+9}_{-12}
	Second approach	
		0.35^{+2}_{-2}
	Third approach	
		0.43^{+2}_{-2}

[3]Note, however, that the experimental value of J does depend on assumptions regarding the mixing of the strange and nonstrange quark states.

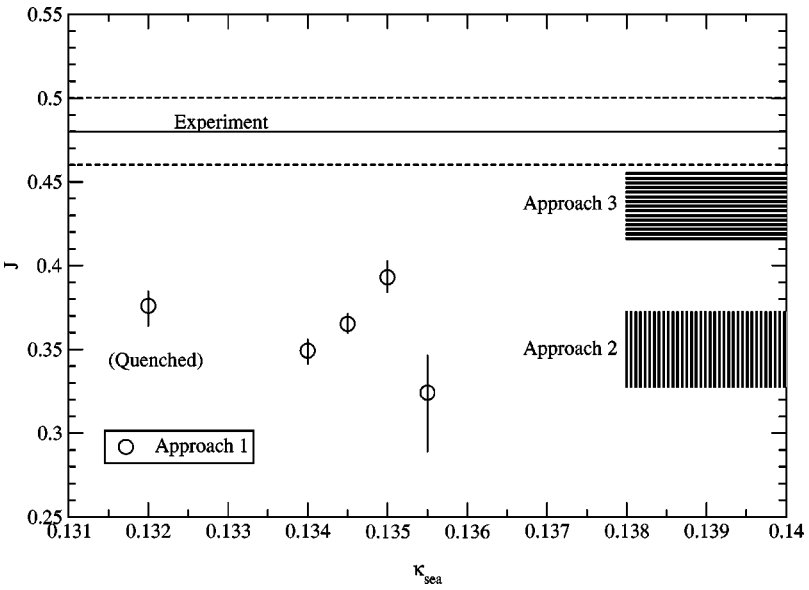

FIG. 7. J versus $\kappa^{\rm sea}$ using the approaches as described in the text. Note that the quenched data points have been plotted at $\kappa^{\rm sea}=0.132$ for convenience. Approaches 2 and 3 are obtained after a chiral extrapolation and are shown as banded regions. The experimental value $J=0.48(2)$ is also shown.

the experimental point as the sea quark mass decreases (see the J value from approaches 1 and 3). This effect will move the lattice estimates of the J parameter towards the experimental value as simulations are performed at more physical values of quark mass.

Recently, there has been a proposed ansatz for the functional form of M_V as a function of $M_{\rm PS}^2$ [47]. However, all our data have $M_{\rm PS}/M_V \gtrsim 0.6$, and for this region, the ansatz of [47] is linear to a good approximation. Therefore, we choose to interpolate our data with a simple linear function and await more chiral data before using the ansatz of [47].

Two groups have recently reported results on the J parameter from dynamical simulations. The CP-PACS Collaboration results at $a \approx 0.11$ fm found $J^{\rm dynamical} > J^{\rm quenched}$ using a clover action [5]. Furthermore, they found that this discrepancy increased as the continuum limit was taken. A similar result was found by the MILC Collaboration, who used an improved staggered action with $a \approx 0.13$ fm [33]. Both of these groups' results match those found in this work.

D. Lattice spacing

In Sec. IV, the lattice spacing a was determined from the intermediate range properties of the static quark potential. In this subsection, we present a complementary determination of a from the meson spectrum.

A common method of determining a from the meson spectrum uses the ρ mass. However, this requires the chiral extrapolation of the vector meson mass down to (almost) the chiral limit. This extrapolation is often performed using a linear function. However, as was discussed in the previous subsection, a linear chiral extrapolation may not be appropriate for $M_V \lesssim 0.8$ GeV. An alternative method of extracting the lattice spacing using the vector meson mass at the *simulated* data points (i.e., without any chiral extrapolation) was given in [48]. Using this method, we obtain the lattice spacing values as shown in Table XIII. Note that these are in general 10–15 % larger than the values from Sec. IV, where the lattice spacing was determined from r_0. A possible explanation for this discrepancy is that the potential and mesonic spectrum are contaminated with different $O(a^2)$ errors, or that the value $r_0=0.49$ fm is 10–15 % too small, and that the true value is $r_0 \approx 0.55$ fm.

It is interesting to study the lattice spacing determinations in more detail since they are a measure of unquenching effects in dynamical simulations. Specifically, it is often assumed that the reason the various quenched determinations of a from, e.g., the meson spectrum differ from that of r_0 or the string tension is due to dynamical quark effects. An obvious quantity to monitor the merging of the various a determinations can be defined as

$$\delta_{i,j}(\beta,\hat{m}_{\rm sea}) = 1 - \frac{a_i(\beta,\hat{m}_{\rm sea})}{a_j(\beta,\hat{m}_{\rm sea})}, \tag{33}$$

where a_i is the lattice spacing determined from the physical quantity $i=\{M_\rho, M_K, f_\pi, \ldots\}$. Obviously, if $\delta_{i,j}=0$, then the lattice prediction for quantity i using the scale determined from j (or vice versa) is in exact agreement with experiment.

Since our simulations are improved to $O(a^2)$, we expect that $\delta \to O(a^2)$ as $m_{\rm sea=val} \to m_l$ (where m_l is the average ud quark mass). Thus a plot of δ against $(\hat{M}_{\rm PS}^{\rm unitary})^{-2}$ would be insightful, where $\hat{M}_{\rm PS}^{\rm unitary}$ is the pseudoscalar mass at the uni-

TABLE XIII. Lattice spacing determined from the mesonic sector using the method of [48].

β	$\kappa^{\rm sea}$	a (Fermi)
5.2000	0.1355	0.110^{+4}_{-3}
5.2000	0.1350	0.115^{+3}_{-3}
5.2600	0.1345	0.118^{+2}_{-2}
5.2900	0.1340	0.116^{+3}_{-4}
5.9300	quenched	0.1186^{+17}_{-15}

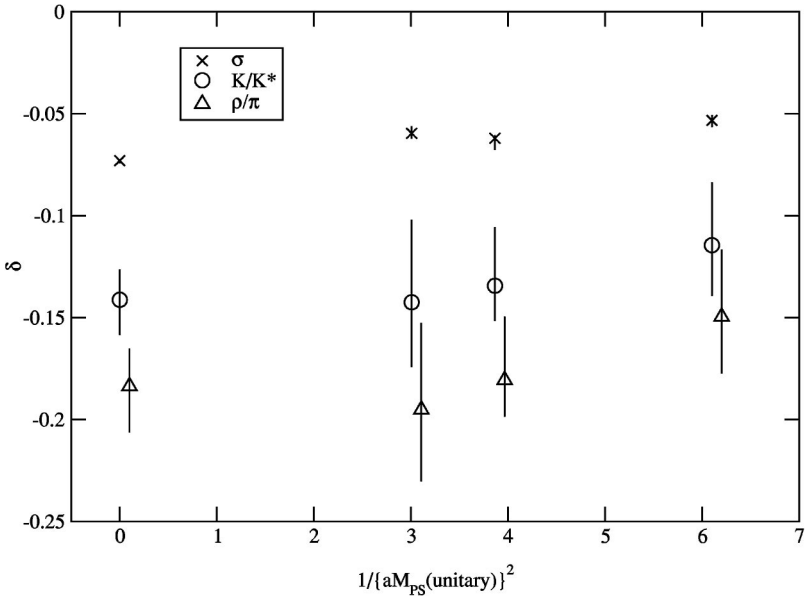

FIG. 8. δ_i as a function of $(1/\hat{M}_{\rm PS}^{\rm deg})^2$ for $i=\sqrt{\sigma}$ and the mass pairs (M_{K*},M_K) and (M_ρ,M_π). δ_i is defined in Eq. (33) with $j=r_0$.

tary point, i.e., for degenerate valence and sea quarks (so $\hat{M}_{\rm PS}^{\rm unitary}=\infty$ for the quenched data). Here, we work with $(\hat{M}_{\rm PS}^{\rm unitary})^{-2}$ rather than $1/\hat{m}_{\rm sea}$ for the x coordinate since it is equivalent to, but easier to define than, $1/\hat{m}_{\rm sea}$. It is important to note that the x coordinate in this plot is the ''control parameter'' for the study of unquenching effects, i.e., when we vary this parameter from its quenched value towards its experimental value, we hope to see the data plotted in the y coordinate move towards its appropriate experimental value. Thus it is easier to interpret unquenching effects directly from this plot than from, e.g., plots of $\hat{M}_V$ against $\hat{M}_{\rm PS}^2$ for various $\hat{m}_{\rm sea}$.

In Fig. 8, $\delta_{i,j}$ is plotted against $(\hat{M}_{\rm PS}^{\rm unitary})^{-2}$ for the matched datasets. In this plot, we have set $j=r_0$ and the various physical quantities i are $\sqrt{\sigma}$ and the hadronic mass pairs (M_{K*},M_K) and (M_ρ,M_π). The method that was used to determine the scale a_i from these mass pairs is that of [48]. It is worth noting that the experimental point on this same plot would occur at an x coordinate of $(\hat{M}_\pi)^{-2}\approx 200$.

Figure 8 does not show signs of unquenching for quantities involving the hadronic spectrum, i.e., the mass pairs (M_{K*},M_K) and (M_ρ,M_π). (Future work will study δ_i for the matrix element quantities $i=f_\pi$ and f_K.) However, there is evidence of unquenching effects when comparing the scale from r_0 with that from $\sqrt{\sigma}$. The quenched value of $\delta_{\sqrt{\sigma}}$ is distinct from the dynamical values, though we note that the method used to obtain σ was optimized for the extraction of r_0 rather than σ itself (see Sec. IV B).

One may wonder if the δ values may have been distorted by not choosing the simulation parameters $(\beta,\hat{m}_{\rm sea})$ exactly on the matched trajectory. In order to obtain a rough estimate of the effect of a mismatched value of β, we use the renormalization group inspired ansatz for a_i [49,50]:

$$a_i(g_0^2)=\Lambda^{-1}f_{\rm PT}(g_0^2)\times[1+X_i f_{\rm PT}(g_0^2)^{n_i}], \qquad (34)$$

where $f_{\rm PT}(g^2)$ is the usual asymptotic scaling function obtained from integrating the β function of QCD and X_i is the coefficient of the $O(a^n)$ lattice systematic. The functional form for $a(g_0^2)$ was originally applied for the quenched theory, but let us assume that it can also be applied in the unquenched case. Using Eq. (34), we see that a mismatch in β of $\Delta\beta$ would lead to a relative error in δ of

$$\frac{\delta(\beta+\Delta\beta)-\delta(\beta)}{\delta(\beta)}\approx -3\Delta\beta. \qquad (35)$$

This shows that even an error in β of as much as $\Delta\beta\approx 0.01$ introduces a relative error in $\delta(\beta)$ of only 3%, ruling out any possible mismatching in β as leading to a significant distortion in δ.

E. Edinburgh plot

In Table XIV, the ratios $M_{\rm PS}/M_V$ are displayed for the case $\kappa^{\rm sea}=\kappa^{\rm val}$. The average u and d quark mass is fixed by requiring $M_{\rm PS}/M_V=0.18$. As can been seen, the simulations are at much larger dynamical quark masses. Figure 9 shows the ''Edinburgh plot'' (M_N/M_V versus $M_{\rm PS}/M_V$) for all the datasets. There is no significant variation within the dynamical data as the sea quark mass is changed, but the dynamical data do tend to lie above the (matched) quenched data. This latter feature may be indicative of finite volume effects since these are expected to be larger in full QCD compared to the quenched case [51]. In [8], an analysis of dynamical finite

TABLE XIV. The ratio $M_{\rm PS}^{\rm unitary}/M_V^{\rm unitary}$ for the dynamical data sets (i.e., with $\kappa\equiv\kappa^{\rm sea}\equiv\kappa^{\rm val}$).

β	κ	$M_{{\rm PS}/M_V}$
5.2000	0.1355	0.578^{+13}_{-19}
5.2000	0.1350	0.700^{+12}_{-10}
5.2600	0.1345	0.783^{+5}_{-5}
5.2900	0.1340	0.835^{+7}_{-7}

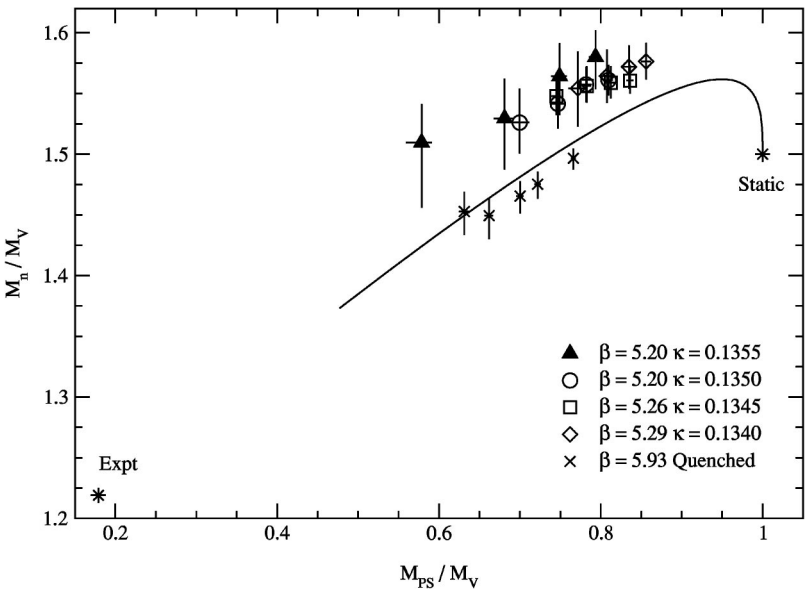

FIG. 9. The Edinburgh plot for all the data sets. All degenerate κ^{val} correlators have been included. The phenomenological curve (from [52]) has been included as a guide to the eye.

volume effects concluded that they were statistically insignificant for spatial extents of $L \gtrsim 1.6$ fm and sea quark masses corresponding to $M_{\mathrm{PS}}/M_V \gtrsim 0.67$ with about 100 configurations. This bound is satisfied for the matched ensembles, but not for the $\kappa^{\mathrm{sea}}=0.1355$ case, where $L=1.60$ fm and $M_{\mathrm{PS}}/M_V=0.58$.

Note also that for heavy valence quark masses, the dynamical data lie close to the phenomenological curve [52], whereas they tend to drift higher than the curve for small valence quark masses. The (matched) quenched data agree well with the curve.

Dynamical results for baryons have recently been reported by two groups. CP-PACS (using a clover action) find good agreement with experiment for strange baryons, but their light baryons (in the continuum limit) are around 10% higher than experiment (see Sec. V C in [5]). They discuss the possibility that this is caused by finite volume effects. The MILC Collaboration (using an improved staggered action) find their dynamical and quenched Edinburgh plots overlay each other [33].

F. Chiral extrapolations

There are a number of different ''chiral extrapolations'' that one can perform in the case of dynamical fermions where there is a two-dimensional quark mass parameter space, $(m_{\mathrm{sea}}, m_{\mathrm{val}})$. We describe three such extrapolations of the data. The first uses a *partially quenched* analysis where each of the m_{sea} datasets is extrapolated entirely separately. The second uses only the *unitary* subset with $m_{\mathrm{sea}} \equiv m_{\mathrm{val}}$. The third does a *combined* fit of all the matched data using a fitting ansatz to model the variation between the different m_{sea} values.

Note that there have been recent proposals for the functional form of M_N and M_V as a function of M_{PS}^2 which go beyond the usual chiral linear ansatz normally used in extrapolations of lattice data [53,47]. However, as reported in Sec. V C, the nonlinearity of these functional forms becomes relevant only for lattice data lighter than in our simulations, and therefore we choose to use naive linear chiral extrapolations in the following.

1. Partially quenched chiral extrapolations

A partially quenched chiral extrapolation was performed for the hadronic masses $\hat{M}=\hat{M}_V$, $\hat{M}_N$, and $\hat{M}_\Delta$ against $\hat{M}_{\mathrm{PS}}^2$, i.e., the following ansatz was used:

$$\hat{M}(\beta,\kappa^{\mathrm{sea}};\kappa^{\mathrm{val}}) = A + B\hat{M}_{\mathrm{PS}}(\beta,\kappa^{\mathrm{sea}};\kappa^{\mathrm{val}})^2. \tag{36}$$

We have introduced the following nomenclature. In $\hat{M}(\beta,\kappa^{\mathrm{sea}};\kappa^{\mathrm{val}})$, the first two arguments refer to the sea parameters: the gauge coupling β and the sea quark mass κ^{sea}. The third argument refers to the valence quark mass κ^{val}. The results for these partially quenched extrapolations appear in Table XV. Note that there is no convincing sign of unquenching effects in that the A and B values for the matched datasets tend to overlay each other, and there is no clear trend for these values as a function of m_{sea}.

Although we choose to extrapolate with respect to $\hat{M}_{\mathrm{PS}}(\beta,\kappa^{\mathrm{sea}};\kappa^{\mathrm{val}})^2$, we also show, for completeness, the values of κ_{crit} in Table XVI. These were obtained from the usual fit of $\hat{M}_{\mathrm{PS}}(\beta,\kappa^{\mathrm{sea}};\kappa^{\mathrm{val}})^2$ versus $1/\kappa^{\mathrm{val}} - 1/\kappa_{\mathrm{crit}}$.

2. Unitary chiral extrapolations

An extrapolation of the hadronic masses $\hat{M}=\hat{M}_V$, $\hat{M}_N$, and $\hat{M}_\Delta$ against $\hat{M}_{\mathrm{PS}}^2$ was performed for the unitary subset of data, i.e., the following ansatz was used:

$$\hat{M}(\beta,\kappa^{\mathrm{sea}};\kappa^{\mathrm{sea}}) = A^{\mathrm{unitary}} + B^{\mathrm{unitary}}\hat{M}_{\mathrm{PS}}(\beta,\kappa^{\mathrm{sea}};\kappa^{\mathrm{sea}})^2, \tag{37}$$

Note that only the matched, dynamical datasets were included in these fits. The results appear in Table XVII.

TABLE XV. The fitting parameters for the partially quenched fit of Eq. (36) for the hadronic masses.

Hadron	β	$\kappa^{\rm sea}$	A	B
Vector meson				
	5.2000	0.1355	0.449^{+21}_{-15}	0.65^{+6}_{-8}
	5.2000	0.1350	0.457^{+11}_{-13}	0.76^{+3}_{-3}
	5.2600	0.1345	0.472^{+7}_{-8}	0.69^{+2}_{-2}
	5.2900	0.1340	0.470^{+15}_{-15}	0.66^{+3}_{-3}
	5.9300	0.0000	0.475^{+9}_{-7}	0.70^{+2}_{-3}
Nucleon				
	5.2000	0.1355	0.653^{+15}_{-17}	1.28^{+9}_{-10}
	5.2000	0.1350	0.67^{+2}_{-2}	1.32^{+6}_{-5}
	5.2600	0.1345	0.72^{+2}_{-2}	1.12^{+4}_{-4}
	5.2900	0.1340	0.71^{+2}_{-2}	1.13^{+4}_{-4}
	5.9300	0.0000	0.653^{+12}_{-12}	1.28^{+4}_{-4}
Delta				
	5.2000	0.1355	0.77^{+4}_{-3}	1.12^{+14}_{-14}
	5.2000	0.1350	0.81^{+3}_{-3}	1.13^{+7}_{-7}
	5.2600	0.1345	0.80^{+2}_{-2}	1.06^{+5}_{-5}
	5.2900	0.1340	0.84^{+2}_{-2}	0.95^{+4}_{-3}
	5.9300	0.0000	0.81^{+2}_{-2}	1.08^{+5}_{-6}

3. Combined chiral fits

It is instructive to perform a combined chiral fit to the entire matched dataset. In order to achieve this, we consider the following fitting ansatz for the fitting of the hadronic mass $\hat{M}$, where

$$\begin{aligned}\hat{M}(\beta,\kappa^{\rm sea};\kappa^{\rm val}) &= A^{\rm combined}+B^{\rm combined}\hat{M}_{\rm PS}(\beta,\kappa^{\rm sea};\kappa^{\rm val})^2\\ &= A_0+A_1\hat{M}_{\rm PS}(\beta,\kappa^{\rm sea};\kappa^{\rm sea})^{-2}\\ &\quad+[B_0+B_1\hat{M}_{\rm PS}(\beta,\kappa^{\rm sea};\kappa^{\rm sea})^{-2}]\\ &\quad\times\hat{M}_{\rm PS}(\beta,\kappa^{\rm sea};\kappa^{\rm val})^2. \qquad (38)\end{aligned}$$

TABLE XVI. Values of $\kappa_{\rm crit}$ obtained for all the datasets.

β	$\kappa^{\rm sea}$	$\kappa_{\rm crit}$
5.20	0.1355	0.13645^{+3}_{-3}
5.20	0.1350	0.13663^{+5}_{-6}
5.26	0.1345	0.13709^{+3}_{-2}
5.29	0.1340	0.13730^{+3}_{-3}
5.93	quenched	0.135202^{+11}_{-11}

TABLE XVII. The fitting parameters for the ''unitary'' dataset fit of Eq. (37) for the hadronic masses.

Hadron	$A^{\rm unitary}$	$B^{\rm unitary}$
Vector meson	0.476^{+14}_{-18}	0.66^{+6}_{-5}
Nucleon	0.69^{+2}_{-3}	1.20^{+9}_{-8}
Delta	0.84^{+3}_{-3}	0.94^{+12}_{-11}

One advantage of such a fitting procedure is that in total, to fit the entire matched dataset, there are fewer fitting parameters than are required in the partially quenched analysis. The functional form in Eq. (38) is the simplest functional form which allows for a variation of A and B with the sea quark mass, and which is finite for all the datasets studied. [Note that $\hat{M}_{\rm PS}(\beta,\kappa^{\rm sea};\kappa^{\rm sea})\equiv\infty$ for the quenched data.] The other advantage is that the parameters A_1 and B_1 are a direct measure of unquenching effects.

The results for the fitting parameters $A_{0,1}$ and $B_{0,1}$ are displayed in Table XVIII for the hadronic masses $\hat{M}_V$, $\hat{M}_N$, and $\hat{M}_\Delta$. The parameters A_1 and B_1 for all the hadrons are compatible with zero at the 2σ level, underlining again the fact that we have not unambiguously uncovered unquenching effects in the meson and baryon spectra.

G. Glueballs and torelons

Experiment has not so far detected glueball states unambiguously in the light hadron spectrum. This failure is usually believed to be a consequence of mixing between the light glueballs and $q\bar{q}$ states (''quarkonia'') with the same quantum numbers and similar masses. We lack, however, a clear understanding of the mixing matrix elements that lead to the strong interaction eigenstates that would be observed, and thus phenomenological attempts to describe the content (gluonic or quarkonium) of the scalar sector glueball candidates have led to widely differing results [54,55].

Lattice QCD can in principle predict these mixing parameters, and in the quenched approximation precise values are known for the continuum gluodynamics (quenched QCD) glueball masses (see [56,57] for reviews). Attempts to measure the mixing matrix have been made (see [57] for a review of quenched measurements, and [58] for first determinations in the presence of sea quarks) and are in progress using the current UKQCD field configurations [59]. Simultaneously, the validity of such a simple mixing scenario can also be addressed [60].

TABLE XVIII. The fitting parameters for the combined fit of Eq. (38) for the hadronic masses.

Hadron	A_0	A_1	B_0	B_1
Vector meson	0.492^{+10}_{-9}	-0.004^{+2}_{-3}	0.61^{+4}_{-4}	0.015^{+9}_{-7}
Nucleon	0.663^{+13}_{-15}	0.006^{+3}_{-4}	1.23^{+6}_{-6}	-0.001^{+1}_{-1}
Delta	0.84^{+2}_{-2}	-0.002^{+5}_{-5}	0.91^{+8}_{-9}	0.02^{+2}_{-2}

Quenched glueball calculations require large ensembles and, until recently, it had been assumed that a similar level of statistical noise would preclude accurate measurements in simulations with dynamical fermions. We find, however, in common with other recent studies [31] that statistical errors are, somewhat surprisingly, reduced in dynamical simulation estimates of glueball masses at present parameter values, at least compared to similarly sized quenched ensembles.

Before continuing with a discussion of our calculations, we need to be a little more specific about what we mean when we talk of ''glueballs'' in QCD. The point is that the presence of quarks will change the vacuum and there is no fundamental reason to think that the mass spectrum of QCD can be approximately described as consisting of the glueballs of the pure gauge theory, the usual quarkonia, and, where these are close in mass, mixtures of the two. There is, however, a collection of phenomena—the Okubo-Zweig-Iizuka (OZI) rule, small sea quark effects, etc.—that creates a reasonable prejudice that this might be so. This question will be examined more explicitly elsewhere [60]. Here we shall follow the usual view and assume it to be so. In that case, we expect that if there are no nearby quarkonia, then the states most readily visible using purely gluonic operators similar to those used in pure gauge theories will be almost entirely glueball-like. This is (probably) the case for the scalar ''glueball'' state we discuss herein. The fact that the overlap of this state onto these purely gluonic operators is similar to that in the pure gauge theory reinforces our prejudice. Thus we will refer to this state as the scalar glueball during the remainder of our analysis.

If we then assume that the glueball spectrum of the dynamical theory is not radically different from that of the pure gauge gluodynamics, we expect the lightest states to be the scalar and tensor ground states. In terms of the reduced symmetries of the space-time lattice, these correspond to the A_1^{++} and T_2^{++} representations of the appropriate cubic group. In the continuum where full rotational symmetry is restored, these match onto the $J^{\mathrm{PC}}=0^{++},2^{++}$ states. Given the size of our ensembles, we find it difficult to resolve lattice masses much beyond $\hat{M}_G \sim 1.2$. In gluodynamics, the heavier tensor state has a (continuum extrapolated) mass in units of the Sommer scale around $r_0 M_G \simeq 6$. The $\hat{r}_0$ values tabulated for our ensembles in Table V thus suggest that the scalar and tensor are the states we will most likely be able to study.

Using a full arsenal of noise reduction techniques, it is now possible to make good estimates of the masses of these lightest glueball masses using existing ensembles. In this section, we present, as an example, the scalar and tensor states extracted from one ensemble, that at $(\beta,\kappa) = (5.20, 0.135\,50)$. Full results for all couplings, and giving greater details of methodology, will be reported in [60]. Preliminary results have appeared in [14].

Measurements were made after every tenth (HMC) trajectory giving an ensemble of 830 configurations, which may not be uncorrelated. A jack-knife error analysis was performed using ten bins, each 830 trajectories in size, which were much larger than the autocorrelation times of the observables. This ensured statistically uncorrelated averages for neighboring bins.

To reduce statistical errors on mass estimates, operators should have a good overlap onto the ground-state excitation with the specified quantum numbers. This was achieved in two ways.

Each operator is based on a traced, closed contour of gauge links, which is gauge-invariant. We may improve the overlap of these operators onto the ground-state excitations by ''smearing'' and ''blocking'' the links. The former is computationally cheap, but the latter has the advantage of doubling the spatial extent of the operator with each iteration. This proves especially useful for measuring wave functions that are not spherically symmetric, such as the tensor. The details of this procedure will be discussed further in [60].

A suite of four glueball operators was constructed in each time slice of the gauge field configurations by summing similarly improved contours in the appropriate symmetry combinations [61]. Overall this gave 28 operators per symmetry channel. These were cross-correlated and a Lüscher-Wolff variational analysis [62] (for details of the exact procedure, see Sec. 3.2 of [63]) used to extract the ground states for each of the lowest momentum combinations of the operators (labeled as $P\cdot P=0,1,\ldots$, where $P\equiv\hat{p}=pa$). All scalar operators (A_1^{++}), for example, were found to have a good overlap (typically greater than 0.7) onto the ground state. The robustness of the variational analysis was checked by examining the behavior of individual correlation functions, and of subsets of the full operator basis. In each case, the mass estimates were found to be consistent as expected given the good overlap of all operators onto the ground state.

From correlation functions we may define an effective energy as a function of the Euclidean timelike separation t (in lattice units) of the creation and annihilation operators:

$$\hat{E}_{\mathrm{eff}}(t) \equiv -\log \frac{\langle \mathcal{O}^{\dagger}(t+1)\mathcal{O}(0)\rangle}{\langle \mathcal{O}^{\dagger}(t)\mathcal{O}(0)\rangle}. \tag{39}$$

The effective energies of the nonzero momentum states were converted to effective masses assuming the lattice dispersion relation

$$\hat{E}(P)^2 = \hat{M}^2 + \sum_{\mu=1}^{3} \sin^2\left(\frac{2\pi P_\mu}{L}\right). \tag{40}$$

The signal from the $P\cdot P=1$ channel was found to be particularly useful. The mass of the ground-state excitation was still small enough for reliable effective energy plateaus to be observed, and statistical noise was observed to be only of a similar magnitude to the $P\cdot P=0$ channel. For $P\cdot P=2$, however, the energies of the states were too large to be confidently assessed. Where they could be extracted, they showed effective-mass plateaus consistent with lower momentum channels. Since they did not improve the quality of the fits, however, they were not included. Correlated and uncorrelated plateau fits were then carried out using $P\cdot P=0,1$ together. As the former fits differed only within errors, for robustness we quote uncorrelated results in this summary.

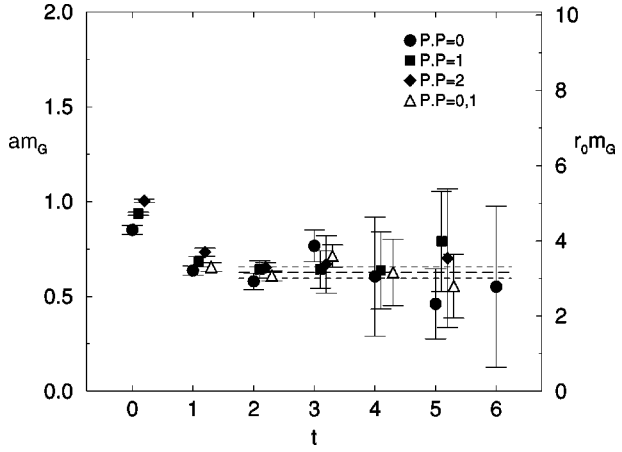

FIG. 10. Effective masses for the A_1^{++} ground state on the $(\beta,\kappa)=(5.20,0.135\,50)$ ensemble.

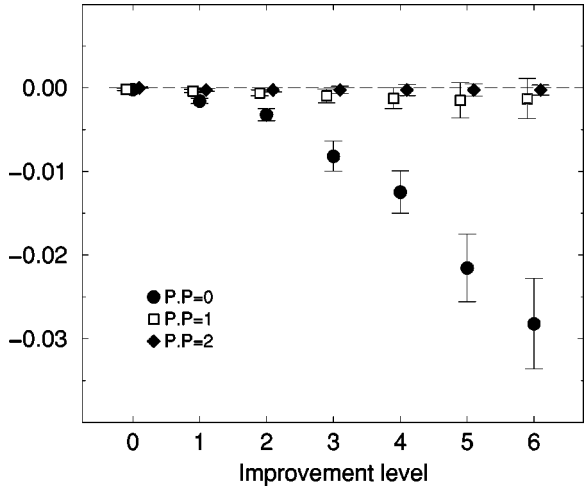

FIG. 11. Vacuum expectation values for Polyakov loops at various blocking levels on the $(\beta,\kappa)=(5.20,0.135\,50)$ ensemble.

In Fig. 10, we plot the effective masses for the various momentum channels of the scalar glueball. A clear plateau is seen in each of the momentum channels. Since these plateaux are compatible, indicating a restoration of the continuum Lorentz symmetry, we can combine the lowest momentum channels to estimate the pure scalar glueball mass $\hat{M}_G=0.628\ (30)$ in lattice units, or $r_0M_G=3.17\ (15)$ in units of the Sommer scale. We note here that the interpolated quenched glueball mass at this lattice spacing is $r_0M_G=3.79\ (16)$ [60], which is significantly above the scalar mass measured here. There would thus appear to be strong evidence for a quenching effect in the scalar glueball channel of QCD. We should temper this statement slightly, as there are other possible sources of suppression of the scalar glueball mass. First, there are finite volume effects which are known to suppress the scalar glueball mass. In quenched QCD, the principle source of this suppression is the mixing of the glueball with torelon pair states, e.g., [64], but we shall demonstrate below that in the present case our lattices are large enough for any such effects to be very small.

More seriously, we do not know the size of this effect in the continuum limit. In the quenched theory, there are known to be large scaling violations in the A_1^{++} channel for the Wilson action [65] with the ''scalar dip'' tending to suppress the mass below the continuum value even at relatively small lattice spacings. Without a continuum limit extrapolation of the glueball mass, we cannot speculate here as to the size of the corresponding effect in the presence of dynamical fermions, but preliminary work suggests the scalar dip may indeed be enhanced in the ensemble considered here [66].

A similar analysis yields a tensor mass estimate of $\hat{M}_G=1.28\ (9)$ in lattice units, or $r_0M_G=6.43\ (42)$ in units of the Sommer scale. This is compatible with the interpolated mass in the pure glue theory $r_0M_G=5.91\ (23)$.

Color flux tubes, analogous to that between a static quark and antiquark pair but without source or sink, can exist on a periodic volume. Rather, the flux tube closes on itself through a spatial boundary (assuming it to be in the ''confined'' phase), forming what is usually termed a torelon. To a first approximation, the mass of the lightest such state equals the spatial extent of the lattice multiplied by the energy per unit length of the flux tube (the string tension). In the infinite volume limit, such states become very massive and decouple from the observed spectrum.

The vacuum expectation value (VEV) of the Polyakov operator that couples to such a torelon loop is zero in the confined phase of gluodynamics, as the loop cannot be broken when no sources in the fundamental representation exist. Thus, only a combination of at least two torelons with the appropriate symmetries can couple to the particle states in the theory. On lattices small enough that the mass of the lightest torelon pair is comparable to the scalar glueball mass, we will see significant finite volume effects.

When light dynamical quarks are present, the torelon becomes unstable to decay. In this case, the Polyakov loop operator gains a nonzero expectation value. This is an effect analogous to the string breaking seen in the static quark potential measured using Wilson loops, and is another explicit signal for the presence of light dynamical quarks in these simulations. In addition, it becomes possible for torelon states to mix with glueballs. Such states are, of course, lighter than the pairs of torelons that mix in the quenched theory, and so we might expect to see finite volume effects on larger lattices in the presence of dynamical quarks.

The Polyakov loop operator is defined as the traced product of links in a line through the periodic spatial boundary:

$$p_\mu(n)=\mathrm{Tr}\prod_{k=1}^{L} U_\mu(n+k\hat{\mu}) \tag{41}$$

for $\mu=1,\ldots,3$. In order to improve statistics, we create a basis of operators using improved spatial links as before.

In Fig. 11, we plot the vacuum expectation value of the $P\cdot P=0,1,2$ Polyakov loop operators. From momentum conservation, we expect the VEVs of the nonzero momentum operators to be zero. This is seen to be satisfied within fewer than two standard deviations in all cases, indicating that the statistical errors are under control. It also adds significance to the fact that the $P\cdot P=0$ operators have a vacuum expecta-

tion value that deviates substantially from zero. This is clear evidence of flux tube breaking by dynamical quark pair production.

Fitting effective masses from $P \cdot P = 0,1$ after a Lüscher-Wolff analysis as before, we estimate the torelon mass as $\hat{M}_P = 0.77$ (5). Including the leading-order universal string correction [67], we expect the loop mass to vary with the lattice size in D dimensions as

$$\hat{M}_P = \sigma L - \frac{\pi(D-2)}{6L}. \tag{42}$$

From this, we estimate the string tension to be $\hat{\sigma} = 0.052$ (3) or, using the Sommer scale to set physical units, $\sqrt{\sigma} = 462$ (13) MeV, in good agreement with the value quoted in Table V.

The mass of the lightest torelon pair, around twice the torelon mass, is thus clearly too heavy to induce finite volume effects. Likewise, finite volume effects from meson exchange through the boundary should be small, although we do not consider this process here. The mass of the torelon, on the other hand, is not much larger than that of the scalar glueball, and there is a possibility of mixing occurring between the two which would lead to a finite volume contamination. We thus perform a variational analysis where we cross-correlate a basis of eight of the ''best'' scalar glueball operators with the two ''best'' torelon operators. We find the matrix to be block-diagonal within errors, and the two lowest eigenstates match closely the original glueball and torelon in mass and operator overlap. Thus this finite volume contamination is negligible, something which could have been anticipated from the small size of the Polyakov line VEV.

In summary, we have presented measurements of the scalar and tensor glueball and torelon masses on an ensemble of configurations at $(\beta, \kappa) = (5.20, 0.135\,50)$. We find clear signals for the presence of light sea quarks, both in a scalar glueball mass that is significantly suppressed below the quenched value at a comparable lattice spacing, and in the breaking of the confining flux tube as demonstrated by a nonzero expectation value for the spatial Polyakov loop operator. Although nonzero, the smallness of these VEVs together with the fact that the torelon and torelon pair masses are significantly larger than the scalar glueball mass lead us to believe that the suppression of the scalar glueball mass is not a finite volume effect, a conclusion which is reinforced by an explicit mixing analysis. The dependence of these effects on the sea quark mass, and whether this effect persists in the continuum limit, is not, however, resolved here.

VI. THE TOPOLOGICAL SUSCEPTIBILITY AND f_π

The ability to access the nonperturbative sectors, and to vary parameters fixed in Nature, has made lattice Monte Carlo simulation a valuable tool for investigating the role of topological excitations in QCD and related theories, and it is these that we now consider.

In quenched lattice calculations, the continuum topological susceptibility now appears to be relatively free of the systematic errors arising from the discretization, the finite volumes, and the various measurement algorithms employed. Attempts to measure the microscopic topological structure of the vacuum are also well advanced (for a recent review, see [68]). The inclusion of sea quarks in lattice simulations, even at the relatively large quark masses currently employed, is numerically extremely expensive, and to avoid significant finite volume contamination of the results, the lattice must be relatively coarse, with a spacing $a \simeq 0.1$ fm as in this study. Compared to quenched lattice studies at least, this is a significant fraction of the mean instanton radius, and has so far precluded a robust, detailed study of the local topological features of the vacuum in the presence of sea quarks. The topological susceptibility, on the other hand, may be calculated with some confidence and provides one of the first opportunities to test some of the more interesting predictions for QCD. Indeed, it is in these measurements that we find some of the most striking evidence for the effects of sea quarks (or, alternatively, for a strong quenching effect) in the lattice simulations described in this paper.

We find clear evidence for the expected suppression of the topological susceptibility in the chiral limit, despite our relatively large quark masses. From this behavior, we can directly estimate the pion decay constant without needing to know the lattice operator renormalization factors that arise in more conventional calculations.

These results were presented at the IOP2000 [13], the Confinement IV [15], and, in a much more preliminary form, the Lattice '99 [12] conferences. Since then, we have increased the size of several ensembles and included a new parameter set. We also have more accurate results from the quenched theory with which to compare. Related results have been presented by the CP-PACS Collaboration [69–71], the Pisa Group [72,73], the SESAM-TχL Collaboration [74], and the Boulder Group [75]. A detailed analysis of our dataset, and its relation to these other studies, will be given in [76].

The topological charge is

$$Q = \frac{1}{32\pi^2} \int d^4x \tfrac{1}{2} \varepsilon_{\mu\nu\sigma\tau} F^a_{\mu\nu}(x) F^a_{\sigma\tau}(x). \tag{43}$$

The topological susceptibility is the squared expectation value of the topological charge, normalized by the volume,

$$\chi = \frac{\langle Q^2 \rangle}{V}. \tag{44}$$

Sea quarks induce an instanton–anti-instanton attraction which in the chiral limit becomes stronger, suppressing Q and χ [77],

$$\chi = \Sigma \left(\frac{1}{m_u} + \frac{1}{m_d} \right)^{-1}, \tag{45}$$

where

$$\Sigma = - \lim_{m_q \to 0} \lim_{V \to \infty} \langle 0 | \bar{\psi} \psi | 0 \rangle \tag{46}$$

is the chiral condensate [78]. We assume $\langle 0|\bar{\psi}\psi|0\rangle = \langle 0|\bar{u}u|0\rangle = \langle 0|\bar{d}d|0\rangle$ and neglect contributions of heavier quarks. The Gell-Mann–Oakes–Renner relation

$$f_\pi^2 M_\pi^2 = 2(m_u + m_d)\Sigma + O(m_q^2) \tag{47}$$

implies

$$\chi = \frac{f_\pi^2 M_\pi^2}{4N_f} + O(M_\pi^4) \tag{48}$$

for N_f degenerate light flavors, in a convention where the experimental value of the pion decay constant[4] $f_\pi \simeq 132$ MeV. Equation (48) holds in the limit $f_\pi^2 M_\pi^2 V \gg 1$, which is satisfied by all our lattices. The higher-order terms ensure that $\chi \to \chi^{\rm qu}$, the quenched value, as $m_q, M_\pi \to \infty$. We find, however, that our measured values are not very much smaller than $\chi^{\rm qu}$, so we must consider two possibilities.

First, there are phenomenological reasons [79,80] for believing that QCD is ''close'' to $N_c = \infty$, and in the case of gluodynamics even SU(2) is demonstrably close to SU(∞) [64,56,81]. Fermion effects are nonleading in N_c, so we expect $\chi \to \chi^{\rm qu}$ for any fixed value of m_q as the number of colors $N_c \to \infty$. For small m_q, we expect

$$\chi = \frac{\chi^\infty M_\pi^2}{\dfrac{4N_f\chi^\infty}{f_\infty^2} + M_\pi^2}, \tag{49}$$

with χ^∞, f_∞ the quantities at leading order in N_c [78]. Alternatively, our $m_q \simeq m_{\rm strange}$ and perhaps higher-order terms are important. In the absence of a QCD prediction,

$$\chi = \frac{f_\pi^2}{2\pi N_f} M_\pi^2 \arctan\left(\frac{2\pi N_f}{f_\pi^2}\chi^{\rm qu}\frac{1}{M_\pi^2}\right) \tag{50}$$

interpolates between Eq. (48) and the quenched limit.[5] Measurements of χ were made on a number of ensembles of $N_f = 2$ lattice field configurations. We reiterate here that these ensembles have two notable features. The improvement is fully nonperturbative, with discretization errors being quadratic rather than linear in the lattice spacing. Second, the couplings are chosen to maintain an approximately constant lattice spacing (as defined by the Sommer scale, $r_0 = 0.49$ fm [9]) as the quark mass is varied. This is important, as the susceptibility in gluodynamics varies considerably with the lattice spacing [56,81], in competition with the variation with m_q. The topological susceptibility is measured from the gauge fields after cooling to remove the UV noise. Further details of the procedure may be found in [13,76].

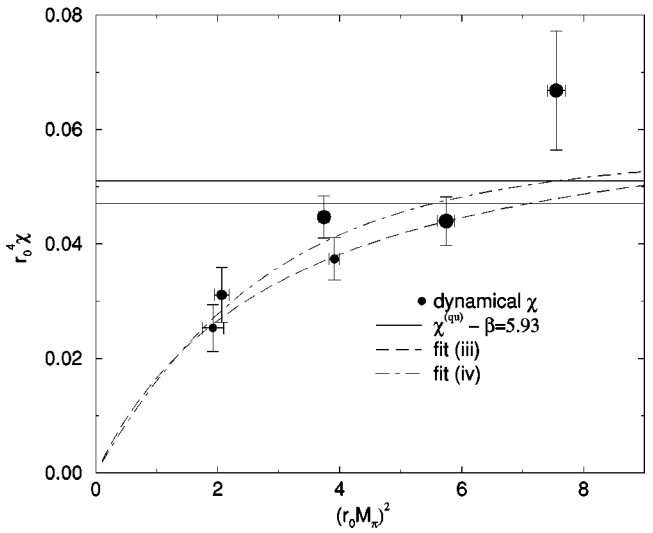

FIG. 12. The measured topological susceptibility, with interpolated quenched points at the same $\hat{r}_0$. The radius of the dynamical plotting points is proportional to $\hat{r}_0^{-1}$. The fits, independent of the quenched points, are (iii) Eq. (53) and (iv) Eq. (54).

We plot data for the ensembles presented in this paper in Figs. 12 and 13, as well as for preliminary results for two further datasets at $(\beta,\kappa) = (5.20, 0.135\,65)$ and $(5.25, 0.135\,20)$. Also shown, as a band, is the interpolated $\chi^{\rm qu}$ at an equivalent lattice spacing. Due to the systematic differences in the methods for determining $\hat{r}_0$ (which can amount to a 20% difference in $\hat{r}_0^4$), the value chosen is for the quenched coupling $\beta = 5.93$, taken from [81], where we have an estimate of $\hat{r}_0$ determined in a consistent manner. The variation in the equivalent quenched susceptibility over the

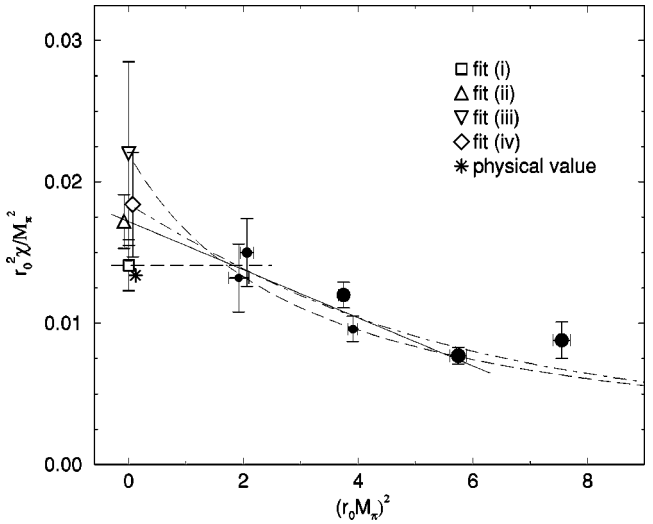

FIG. 13. The measured topological susceptibility. The radius of the dynamical plotting points is proportional to $\hat{r}_0^{-1}$. The fits, independent of the quenched points, are (i) Eq. (51), (ii) Eq. (52), (iii) Eq. (53), and (iv) Eq. (54).

[4]N.B. there is a common alternative convention, used in earlier presentations of these data [13,15], where a factor of 2 is absorbed into f_π^2 in Eq. (48), and where f_π is a factor of $\sqrt{2}$ smaller, around 93 MeV.

[5]Note that, in describing chiral extrapolations, we adopt the common convention of using π to label quantities associated with the pseudoscalar channel irrespective of the quark mass.

range in $\hat{r}_0$ spanned by our data is much smaller than the error on the $\beta=5.93$ point shown, a useful consequence of the matching program.

The behavior of $\hat{r}_0^4\hat{\chi}$ with $(\hat{r}_0\hat{M}_\pi)^2$ is qualitatively as expected and, more quantitatively, we attempt fits motivated by Eqs. (48), (49), and (50). The leading-order chiral behavior will be

$$\frac{\hat{r}_0^2\hat{\chi}}{M_\pi^2}=c_0, \tag{51}$$

with the first correction term generically being

$$\frac{\hat{r}_0^2\hat{\chi}}{M_\pi^2}=c_0+c_1(\hat{r}_0\hat{M}_\pi)^2. \tag{52}$$

Attempting to include data further from the chiral limit, large-N_c theory suggests a functional form

$$\frac{\hat{r}_0^2\hat{\chi}}{M_\pi^2}=\frac{c_0c_3}{c_3+c_0(\hat{r}_0\hat{M}_\pi)^2}, \tag{53}$$

while a more general interpolation is provided by

$$\frac{\hat{r}_0^2\hat{\chi}}{M_\pi^2}=\frac{2c_0}{\pi}\arctan\left(\frac{\pi c_3}{2c_0(\hat{r}_0\hat{M}_\pi)^2}\right). \tag{54}$$

In each case, the intercept is related to the decay constant by $c_0=(\hat{r}_0\hat{f}_\pi)^2/8$. The corresponding fits are shown in Figs. 12 and 13. The extent of the curves indicates which points were included in fit. We include progressively fewer chiral points until the χ^2/d.o.f. of the fit becomes unacceptably bad. We note the wide range fitted simply by including an M_π^4 term, and the consistency of our data with large-N_c predictions. The stability and similarity of the fits motivate us to use c_0 from Eq. (52) to estimate $f_\pi=149\pm8^{+25}_{-14}$ MeV at a lattice spacing $a\simeq0.1$ fm, with variation between other fits providing the second, systematic error, and in good agreement with the experimental value around 132 MeV.

VII. CONCLUSIONS

Two particular features distinguish this work from previous published reports on lattice simulations of QCD with dynamical fermions. It represents the first presentation of a wide range of results using the fully nonperturbatively improved Wilson action. It also demonstrates the value of a new strategy of using so-called ''matched ensembles'' which allows a more controlled study of unquenching effects than would otherwise be possible at finite lattice spacing.

We have presented detailed measurements of the static interquark potential, light hadron spectrum, scalar and tensor glueballs, torelon states, and the topological charge and susceptibility.

From the analysis of these quantities, we have presented significant evidence of effects attributable to dynamical effects (two flavors of light quarks) on the static interquark potential, particularly at short range (Sec. IV C), and the topological susceptibility (Sec. VI).

We have also seen some evidence of dynamical quark effects in the effective string tension (Sec. V D), the nucleon mass (Sec. V E), and the scalar glueball mass (Sec. V G).

For the present range of light quark masses ($M_\pi/M_\rho\gtrsim0.58$), there is no convincing evidence of effects on the light meson spectrum, nor do we see evidence of string breaking, save indirectly in the small, but nonzero, VEV of the winding gluonic flux tube (torelon) operator.

Further analyses of these ensembles and complementary ones being produced by the QCDSF Collaboration [82,83] are underway.

ACKNOWLEDGMENTS

We acknowledge the support of the U.K. Particle Physics and Astronomy Research Council under grants GR/L22744, GR/L29927, GR/L56374, PPA/G/O/1998/00621, and PPA/G/O/1998/00518. A.H. wishes to thank the Aspen Center for Physics for its hospitality during part of this work. H.W. acknowledges the financial support of the PPARC. C.R.A. wishes to thank R.G. Edwards for useful conversations.

[1] S. Güsken, Nucl. Phys. B (Proc. Suppl.) **63**, 16 (1998).
[2] CP-PACS Collaboration, R. Burkhalter *et al.*, Nucl. Phys. B (Proc. Suppl.) **73**, 3 (1999).
[3] R. D. Mawhinney, Nucl. Phys. B (Proc. Suppl.) **83–84**, 57 (2000).
[4] S. Aoki, Nucl. Phys. B (Proc. Suppl.) **94**, 3 (2001).
[5] CP-PACS Collaboration, A. Ali Khan *et al.*, hep-lat/0105015.
[6] R. D. Kenway, Nucl. Phys. B (Proc. Suppl.) **73**, 16 (1999).
[7] ALPHA Collaboration, K. Jansen and R. Sommer, Nucl. Phys. **B530**, 185 (1998).
[8] UKQCD Collaboration, C. R. Allton *et al.*, Phys. Rev. D **60**, 034507 (1999).
[9] R. Sommer, Nucl. Phys. **B411**, 839 (1994).
[10] UKQCD Collaboration, A. C. Irving *et al.*, Phys. Rev. D **58**, 114504 (1998).
[11] UKQCD Collaboration, J. Garden, Nucl. Phys. B (Proc. Suppl.) **83–84**, 165 (2000).
[12] UKQCD Collaboration, A. Hart and M. Teper, Nucl. Phys. B (Proc. Suppl.) **83–84**, 476 (2000).
[13] UKQCD Collaboration, A. Hart and M. Teper, hep-ph/0004180.
[14] UKQCD Collaboration, A. C. Irving, Nucl. Phys. B (Proc. Suppl.) **94**, 242 (2001).
[15] UKQCD Collaboration, A. Hart and M. Teper, talk presented at the Confinement IV conference, Vienna, 2000.
[16] UKQCD Collaboration, C. Allton, hep-lat/0012026.
[17] S. Duane, A. D. Kennedy, B. J. Pendleton, and D. Roweth, Phys. Lett. B **195**, 216 (1987).
[18] B. Sheikholeslami and R. Wohlert, Nucl. Phys. **B259**, 572 (1985).

[19] UKQCD Collaboration, B. Joo *et al.*, Phys. Rev. D **62**, 114501 (2000).
[20] Z. Bai, M. Fahey, and G. Golub, School of Engineering, Stanford University Report No. SCCM-95-09, 1995.
[21] UKQCD Collaboration, E. Cahill, A. Irving, C. Johnson, and J. Sexton, Nucl. Phys. B (Proc. Suppl.) **83–84**, 825 (2000).
[22] R. G. Edwards, U. M. Heller, and T. R. Klassen, Nucl. Phys. **B517**, 377 (1998).
[23] C. Michael, Nucl. Phys. **B259**, 58 (1985).
[24] S. Perantonis, A. Huntley, and C. Michael, Nucl. Phys. **B326**, 544 (1989).
[25] APE, M. Albanese *et al.*, Phys. Lett. B **192**, 163 (1987).
[26] UKQCD Collaboration, H. Wittig, Nucl. Phys. B (Proc. Suppl.) **42**, 288 (1995).
[27] C. Michael, Phys. Lett. B **283**, 103 (1992).
[28] ALPHA Collaboration, M. Guagnelli, R. Sommer, and H. Wittig, Nucl. Phys. **B535**, 389 (1998).
[29] JLQCD Collaboration, S. Aoki *et al.*, Nucl. Phys. B (Proc. Suppl.) **94**, 233 (2001).
[30] M. Luscher, Nucl. Phys. **B180**, 317 (1981).
[31] SESAM Collaboration, G. S. Bali *et al.*, Phys. Rev. D **62**, 054503 (2000).
[32] C. Bernard *et al.*, Phys. Rev. D **62**, 034503 (2000).
[33] C. Bernard *et al.*, Phys. Rev. D **64**, 054506 (2001).
[34] UKQCD Collaboration, C. R. Allton *et al.*, Phys. Rev. D **49**, 474 (1994).
[35] J. Garden, Ph.D. thesis, University of Edinburgh, 2000.
[36] UKQCD Collaboration, P. Lacock, A. McKerrell, C. Michael, I. M. Stopher, and P. W. Stephenson, Phys. Rev. D **51**, 6403 (1995).
[37] C. Michael and A. McKerrell, Phys. Rev. D **51**, 3745 (1995).
[38] B. Efron and R. J. Tibshirani, Science **253**, 390 (1991).
[39] A. Duncan *et al.*, Phys. Rev. D **51**, 5101 (1995).
[40] UKQCD Collaboration, K. C. Bowler *et al.*, Phys. Rev. D **62**, 054506 (2000).
[41] M. Luscher, S. Sint, R. Sommer, and P. Weisz, Nucl. Phys. **B478**, 365 (1996).
[42] M. Luscher and P. Weisz, Nucl. Phys. **B479**, 429 (1996).
[43] UKQCD Collaboration, S. Collins and C. T. H. Davies, Nucl. Phys. B (Proc. Suppl.) **94**, 608 (2001).
[44] T. Bhattacharya, S. Chandrasekharan, R. Gupta, W. Lee, and S. Sharpe, Phys. Lett. B **461**, 79 (1999).
[45] T. Bhattacharya, R. Gupta, W. Lee, and S. Sharpe, Phys. Rev. D **63**, 074505 (2001).
[46] UKQCD Collaboration, P. Lacock and C. Michael, Phys. Rev. D **52**, 5213 (1995).
[47] D. B. Leinweber, A. W. Thomas, K. Tsushima, and S. V. Wright, Phys. Rev. D **64**, 094502 (2001).
[48] C. R. Allton, V. Gimenez, L. Giusti, and F. Rapuano, Nucl. Phys. **B489**, 427 (1997).
[49] C. R. Allton, hep-lat/9610016.
[50] C. R. Allton, Nucl. Phys. B (Proc. Suppl.) **53**, 867 (1997).
[51] A. Ukawa, Nucl. Phys. B (Proc. Suppl.) **30**, 3 (1993).
[52] S. Ono, Phys. Rev. D **17**, 888 (1978).
[53] D. B. Leinweber, A. W. Thomas, K. Tsushima, and S. V. Wright, Phys. Rev. D **61**, 074502 (2000).
[54] F. E. Close and A. Kirk, Eur. Phys. J. C **25**, 531 (2001).
[55] W. Lee and D. Weingarten, Phys. Rev. D **61**, 014015 (2000).
[56] M. Teper, hep-th/9812187.
[57] D. Toussaint, Nucl. Phys. B (Proc. Suppl.) **83**, 151 (2000).
[58] UKQCD Collaboration, C. Michael, M. S. Foster, and C. McNeile, Nucl. Phys. B (Proc. Suppl.) **83**, 185 (2000).
[59] UKQCD Collaboration, C. McNiele and C. Michael, Phys. Rev. D **63**, 114503 (2001).
[60] UKQCD Collaboration, A. Hart and M. Teper, Phys. Rev. D (to be published), hep-lat/0108022.
[61] C. Michael, Acta Phys. Pol. B **21**, 119 (1990).
[62] M. Luescher and U. Wolff, Nucl. Phys. **B339**, 222 (1990).
[63] A. Hart, M. Laine, and O. Philipsen, Nucl. Phys. **B586**, 443 (2000).
[64] M. Teper, Phys. Rev. D **59**, 014512 (1999).
[65] C. J. Morningstar and M. Peardon, Phys. Rev. D **60**, 034509 (1999).
[66] UKQCD Collaboration, A. Hart (unpublished).
[67] P. de Forcrand, G. Schierholz, H. Schneider, and M. Teper, Phys. Lett. **160B**, 137 (1985).
[68] M. Teper, Nucl. Phys. B (Proc. Suppl.) **83–84**, 146 (2000).
[69] CP-PACS Collaboration, A. Ali Khan *et al.*, Nucl. Phys. B (Proc. Suppl.) **83–84**, 162 (2000).
[70] S. Durr, Nucl. Phys. **B611**, 281 (2001).
[71] CP-PACS Collaboration, A. Ali Khan *et al.*, Phys. Rev. D **64**, 114501 (2001).
[72] B. Alles, M. D'Elia, and A. Di Giacomo, Nucl. Phys. B (Proc. Suppl.) **83–84**, 431 (2000).
[73] B. Alles, M. D'Elia, and A. Di Giacomo, Phys. Lett. B **483**, 139 (2000).
[74] G. S. Bali *et al.*, Phys. Rev. D **64**, 054502 (2001).
[75] A. Hasenfratz, Phys. Rev. D **64**, 074503 (2001).
[76] UKQCD Collaboration, A. Hart and M. Teper, hep-lat/0108006.
[77] P. Di Vecchia and G. Veneziano, Nucl. Phys. **B171**, 253 (1980).
[78] H. Leutwyler and A. Smilga, Phys. Rev. D **46**, 5607 (1992).
[79] G. 't Hooft, Nucl. Phys. **B75**, 461 (1974).
[80] E. Witten, Nucl. Phys. **B160**, 57 (1979).
[81] B. Lucini and M. Teper, J. High Energy Phys. **06**, 050 (2001).
[82] QCDSF Collaboration, D. Pleiter, Nucl. Phys. B (Proc. Suppl.) **94**, 265 (2001).
[83] S. Booth *et al.*, Phys. Lett. B **519**, 229 (2001).